



Extrusion kinematics of UHP terrane in a collisional orogen: EBSD and microstructure-based approach from the Tso Morari Crystallines (Ladakh Himalaya)

Dripta Dutta^{*}, Soumyajit Mukherjee

Department of Earth Sciences, Indian Institute of Technology Bombay, Powai, Mumbai 400 076, Maharashtra, India

ARTICLE INFO

Keywords:

Channel flow
Quartz CPO
CVA analysis
Partial melting
Opposite shear
Triclinic flow

ABSTRACT

Several extrusion mechanisms have been proposed to explain the occurrences of ultra-high pressure (UHP) rocks at collisional margins. Here we assess the suitability of the channel flow model of extrusion for the Tso Morari Crystallines (TMC) by investigating the *syn*-extrusion deformation kinematics of the UHP eclogite-bearing gneiss that dominates the TMC. Samples collected from the two transects viz. Sumdo-Karzok and Sumdo-Debring, have been examined. The channel flow model predicts high simple shear component at the channel margins during extrusion. Gneisses near the upper margin of the subduction channel – also the northern margin of the TMC on map – support this claim and exhibit closely spaced shear planes, and elevated fluid activity as revealed by X-ray diffraction results. Quartz grain parameters e.g. Feret diameter, aspect ratio, and vector mean strength measured from oriented thin-sections of the gneiss do not exhibit distinct pattern of variation of deformation intensity across the TMC. EBSD-based low-angle intragranular 'neighbor to neighbor' misorientation analysis and micro-textural evidences of incipient partial melting in the gneiss reflect temperatures >600 °C. We propose that return flow and buoyancy of the subducted continental crust triggered the extrusion, which was then facilitated by the Indo-Eurasia collision. The mechanism could thus be a combination of both channel flow and ductile wedge extrusion. Continued convergence possibly promoted non-planar triclinic transpression – also evident from the *crystallographic vorticity axis* (CVA) analysis – such that the extrusion direction varied spatially, producing the diverse shear senses observed at both meso- and micro-scales.

List of symbols

Symbol	Meaning
α	Angle of obliquity
θ	Angle between the long axis of the quartz grain and the macroscopic foliation (measured anticlockwise)
E	Entropy index
J	Texture index
M	Misorientation index
S	Symmetry value
\bar{a}	Vector mean strength

1. Introduction

Ultra-high pressure (UHP) terranes result from subduction of crustal rocks to >90 km depth and subsequent exhumation/extrusion. They are characterized by a range of structural and petrological features, which can explain the geodynamic processes that produce them. Mechanisms driving their extrusion aid in visualizing their tectonic evolution and thus have been extensively researched for over three decades. Consequently, several terrane-specific models have come up (Supplementary Fig. S1).

The term 'extrusion' has been previously used to refer both vertical (Sizova et al., 2012) or lateral (Hacker et al., 2017) movement of rigid crustal blocks (Johnson and Harley, 2012). Grujic et al. (1996)

Abbreviations: Abbreviation, Full form; BLG, Bulging; BVA, Bulk vorticity axis; CVA, Crystallographic vorticity axis; GBM, Grain boundary migration; GRF, Geographic reference frame; KRF, Kinematic reference frame; OA, Opening angle; OSS, Opposite shear senses; SGR, Subgrain rotation; SRF, Sample reference frame; TMC, Tso Morari Crystallines; UHP, Ultra-high pressure; VNS, Vorticity normal section; ZSZ, Zildat shear zone.

^{*} Corresponding author.

E-mail addresses: dripta.dutta@gmail.com (D. Dutta), smukherjee@iitb.ac.in, soumyajitm@gmail.com (S. Mukherjee).

<https://doi.org/10.1016/j.tecto.2020.228641>

Received 11 July 2020; Received in revised form 1 October 2020; Accepted 6 October 2020

Available online 18 October 2020

0040-1951/© 2020 Elsevier B.V. All rights reserved.

suggested ‘ductile wedge extrusion’ model for the Higher Himalayan Crystallines, where the extruding materials get pervasively deformed. In this work, we use ‘extrusion’ following Grujic et al. (1996) to refer to the approach of the subducted crust towards the surface.

The Tso Morari Crystallines (TMC), which comprises of the UHP eclogite-bearing gneisses (Table 1), occurs as an isolated NW-SE trending dome bound by detachment faults in the NW Trans-Himalaya in India (Fig. 1). The extrusion mechanism for the TMC is debated (Supplementary Fig. S1). For example, Beaumont et al. (2009) proposed a ‘pulse-like’ channel flow model of *syn*-collisional (~ 54 Ma, Najman et al., 2017; ~ 50 Ma, Bhattacharya et al. In Press) extrusion. This happened through a channel (dip ~6° near the trench to ~40° at ~100 km depth: Leech et al., 2005), driven by the buoyant push of the formerly subducted crust. Other models, viz., the ductile extrusion of wedge (Supplementary Fig. S1) by combined coaxial and non-coaxial deformation (Epard and Steck, 2008) and the diapiric ascent (Supplementary Fig. S1) of the UHP crust through a mantle-wedge (Chatterjee and Jagoutz, 2015), are less popular.

The channel flow model (Beaumont et al., 2004; Godin et al., 2006; Harris, 2007; Mukherjee, 2013) predicts: (a) inversion of kinematic indicators such that opposite shear senses (OSS) overprint near the upper and lower boundaries of the channel, (b) general shear (coeval pure and simple shear) of the extruding material under ductile regime, and (c) intense shear at the channel margins and a gradual decline towards the channel center.

Based on numerical modelling, Beaumont et al. (2009) proposed the extrusion mechanism for the TMC (also see Mukherjee and Mulchrone, 2012). However, none of the previous studies on the TMC concluded the same from either a field-based or microstructural perspective. In this study, we investigate the *syn*-extrusion deformation and flow kinematics of the TMC, the gneiss in particular (Fig. 1) to comment on the viability of the channel flow model.

A multi-technique approach has been employed including field-, microstructural and EBSD studies. X-ray diffraction analysis (Section 3.2) is performed to quantify the modal mineralogy of the gneiss across the TMC (Fig. 1). Petrographic studies are conducted to note the micro-textures (Section 3.3.1), decipher deformation temperatures from quartz (Section 3.3.2) and feldspar (Section 3.3.3) microstructures, and identify shear senses (Section 3.3.4). Quartz grain parameters (Section 3.4) viz. Feret diameter, aspect ratio and vector mean strength etc. are quantified from monocrystalline ribbons to detect the variation in deformation intensity across the TMC. EBSD-based quartz (c)-axis study (Section 3.5.1) is employed to confirm the deformation temperatures deduced from petrography, whereas the CVA analysis (Section 3.5.2) is utilized to infer the nature of deformation and the *syn*-extrusion flow kinematics.

2. Geology

The Tso Morari Crystallines (TMC) is located in the Indian Trans-Himalaya to the south of the ~ NW trending Indus-Tsangpo Suture Zone (ITSZ) and has a sub-elliptical outline (dimensions: ~ 100 × 50 × 7 km³) (de Sigoyer et al., 2004). It evolved tectono-thermally (Fig. 2a,c; Supplementary Tables S2-S4) in at least three stages (de Sigoyer et al., 2000; Buchs, 2019) that started with an initial prograde metamorphism (St-Onge et al., 2013) as the Neo-Tethys oceanic lithosphere subducted beneath the Eurasian plate margin. This was followed by UHP (2.24–4.8 GPa, 450–760 °C, Supplementary Table S3) metamorphism at ~53 Ma (Buchs, 2019) and *syn*-collisional extrusion along a NE-dipping subduction channel (Beaumont et al., 2009; Fig. 2b1-b2) (de Sigoyer et al., 2000).

Detachment faults separate the TMC from the ITSZ in the north (Figs. 1, 3a,b) and the Tethyan succession in the south (Wilke et al., 2015). Stratigraphically, the TMC consists of the Tso Morari Gneiss overlain by the meta-sedimentary sequence (Table 1). The I-type Rupshu (~ 482 Ma.) granite occurs as an intrusive (Table 1) and is much less deformed than the gneiss (Sachan et al., 2005). The S-type Polokongka

La granite (~ 479 Ma; Gouzu et al., 2006) – protolith to the gneiss – was intruded by basic dykes. These dykes underwent UHP metamorphism at >90 km depth and got eclogitized. However, the granite being anhydrous (Palin et al., 2017), stayed stable over wider P-T conditions. The rapid burial and extrusion inhibited its eclogitization (de Sigoyer et al., 2004). The gneisses host foliation-parallel garnetiferous eclogite (kyanite-sillimanite grade) boudins. Also, EBSD-based identification of the coesite → quartz transformation has recently been reported from the Polokongka La granite (Bidgood et al., 2020).

Epard and Steck (2008) identified four *syn*-extrusional deformation phases and overprinting of schistosity (Supplementary Table S2). However, the authors collectively term them as the “main schistosity” (S; fig. 2 of Epard and Steck, 2008) that exhibits a sub-horizontal attitude throughout the gneiss. This observation matches with the S2 foliations of both Guillot et al. (1997) and de Sigoyer et al. (2004). The latter further advocated that the penultimate D2 deformation phase (also *syn*-extrusional; fig. 6 of de Sigoyer et al., 2004; Supplementary Table S2) is the major one that affected the gneissic rocks. It was followed by a weaker D3, restricted to the northern and the southern peripheries only. Hence, we consider the dominant foliation/schistosity (S2 of de Sigoyer et al., 2004; S of Epard and Steck, 2008) observed in the gneiss and discussed throughout the text to be *syn*-extrusional as well.

3. Methodologies & results

3.1. Field observations

Fieldwork has been carried out along two transects: A) Sumdo-Karzok (~ 50 km), and B) Sumdo-Debring (~ 62 km) (Fig. 1). The mylonitized and schistose rocks near the Zildat Shear Zone (ZSZ), have closely spaced shear planes (Fig. 3c-j), and appear to be more intensely deformed than those present at the centre of the TMC (also see Supplementary Fig. S3). The foliations are sub-horizontal to gently dipping throughout, except at the peripheries (Locations 6 and 14: Fig. 4). Within the gneiss, they locally define the C-planes.

The brittle primary shear Y-planes at the N margin of the TMC cross-cut (~ 50–60°) the foliations (Fig. 3c-f) and exhibit conflicting brittle shear senses – both *top-down-to-N* and *top-up-to-S*. This is the first report of a possible brittle reactivation of the fault with an opposite slip. Near-vertical, ~ NE-SW striking fractures (Fig. 4) occur throughout the Tso Morari gneiss (Supplementary Fig. S3).

Sub-horizontal (plunge amount: 4–20°) stretching lineations defined by aligned muscovites and biotites (Fig. 4) are noted in the field. Majority of them plunge towards NE/E. A few locations (6, 11, 16, 18, and 20: Supplementary Fig. S4) exhibit two sets, of which one is more prominent (*L_a*: more prominent; *L_b*: less prominent). However, no cross-cut relation exists between the two in the field or in the hand specimens, possibly implying their coeval development. Each of the rest of the locations show a single set, which varies from one location to another (Fig. 4). Previous works on this area e.g., Guillot et al. (1997), de Sigoyer et al. (2004), Epard and Steck (2008), report at least 3 sets of stretching lineations from the gneiss, and establish all of them to be *syn*-extrusional (Supplementary Table S2). The orientations of the lineations observed in this study, closely match with those reported by de Sigoyer et al. (2004) – ‘L2’ of the strongest ‘D2’ (~ 55–47 Ma) phase that are sub-horizontal throughout and trend NW-SE in the central part of the TMC, and NE-SW in the northern and southern portions. Hence, we consider the ones reported in this study to be products of the strongest *syn*-extrusional deformation event as well. Whether or not an earlier stretching lineation reoriented during the later weaker deformation event is beyond the scope of this study. However, as proposed by de Sigoyer et al. (2004), the D3 phase was much less intense and was primarily concentrated along the periphery of the TMC.

Table 1

Lithotectonic succession of the Tso Morari Crystallines and the nearby region. The name of the lithounits are in *italics*, and their respective ages are provided below the names within brackets. Compiled from a: [Buchs and Epard \(2019\)](#); b: [Epard and Steck \(2008\)](#), c: [Girard and Bussy \(1999\)](#), d: [Steck et al. \(1998\)](#), e: [Fuchs and Linner \(1996\)](#), f: [Thakur and Misra \(1984\)](#), g: [Thakur and Viridi \(1979\)](#). The columns show the different nomenclatures used by previous workers (*referred to as superscripts*) for the lithounits in the terrane. Samples in this study are collected from the unit highlighted in Yellow.

Lamayuru Unit and Tso Morari Dome ^e , North Himalayan Nappes ^{a,b,d}	<i>Indus – Tsangpo Suture Zone</i> ^{a,b}		<i>Nidar Ophiolite</i> (Lower Cretaceous ^{a,f})	<i>Ophiolites</i> (<i>This Study, Fig. 1</i>)	<i>Tso Morari Crystallines (TMC, This Study, Fig. 1)</i>	
			<i>Drakkarpo Nappe</i> ^g (Upper Cretaceous – Lower Eocene ^{a,e})			
			<i>Mata-Nyimaling-Tsarap Nappe</i> (Cambrian – Upper Cretaceous ^d)	<i>Mata Nappe</i> (<i>This Study, Fig. 1</i>)		
			<i>Karzok-Ribil Nappe</i> ^g (Late Cretaceous? ^a)	<i>Tetraogal Nappe</i> (<i>This Study, Fig. 1</i>)		
	<i>Tso Morari Crystallines</i> ^{f,g}	<i>Taglang La Formation</i> (Carboniferous – Permian ^f)	<i>Tso Morari Nappe</i> ^{a,b,d}	<i>Tetraogal Nappe</i> (Permo-Mesozoic ^d)		<i>Metasedimentary rocks</i> (<i>This Study, Fig. 1</i>)
				<i>Karsha Formation</i> (Middle Cambrian ^{a,b})		
				<i>Phe Formation</i> (Late Precambrian – early Middle Cambrian ^{a,b})		
	<i>Puga Formation</i> (Lower Paleozoic – Late Precambrian ^f)		<i>Tso Morari Gneiss</i> [#] (Cambro – Ordovician ^c)	<i>Tso Morari Gneiss</i> (<i>This Study, Fig. 1</i>)		

Notes: #: also referred to as 'Tso Morari Granite' by [Epard and Steck \(2008\)](#) and [Buchs and Epard \(2019\)](#);

%: The Karzok-Ribil Nappe comprises of Karzok Ophiolites (exposed to the south of the TMC) and Ribil unit (exposed to the north of the TMC; [de Sigoyer et al., 2004](#)). The Mata Nappe does not crop out to the north of the TMC and thus the Ribil unit (RU) is overlain by the Drakkarpo Nappe (DN; also known as the Drakkarpo unit; [de Sigoyer et al., 2004](#)). [Thakur and Viridi \(1979\)](#) and [Steck et al. \(1998\)](#), grouped RU and DN into Zildat Ophiolitic Mélange and Sumdo Complex, respectively.

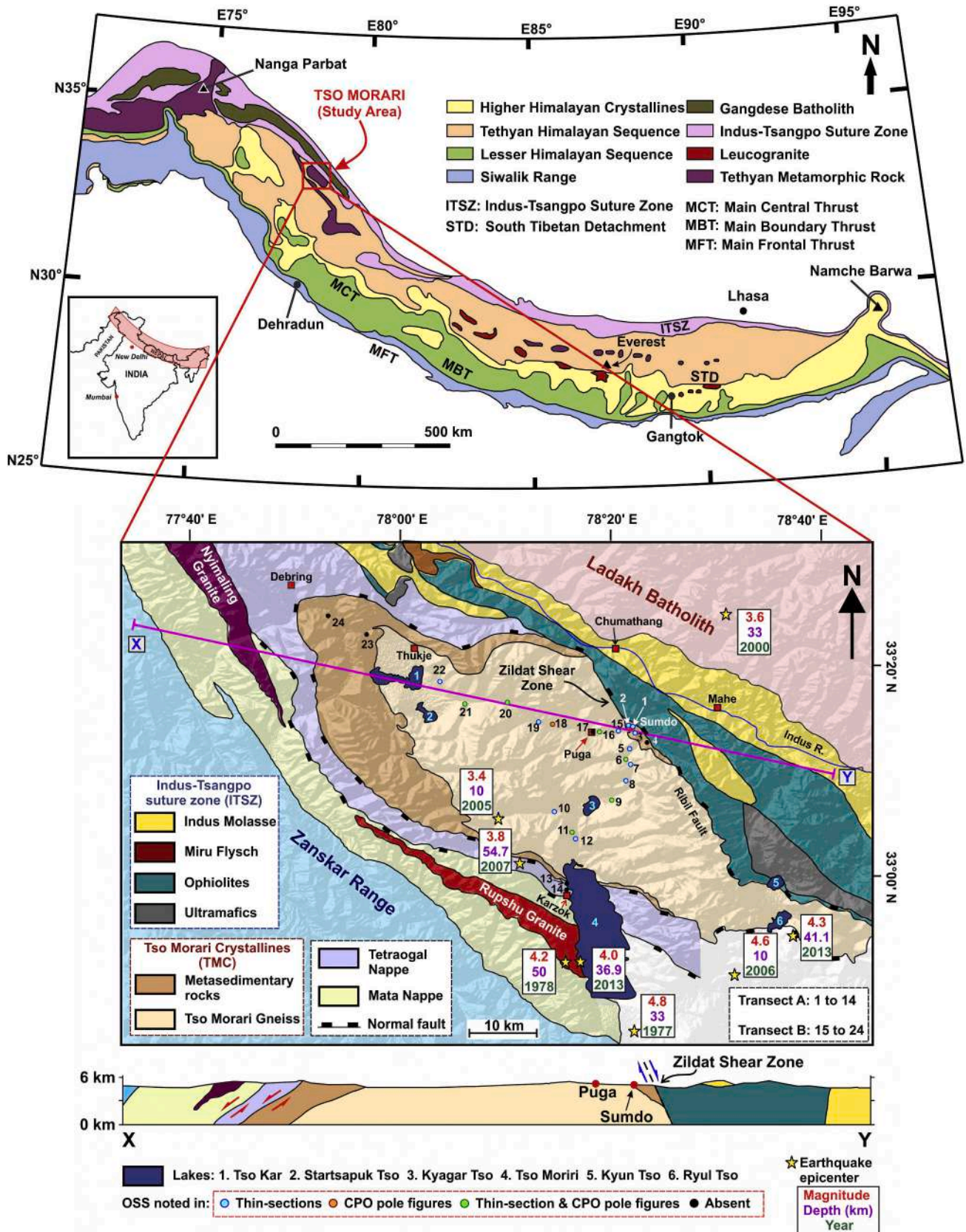


Fig. 1. Geological map of the Himalaya (reproduced from fig. 1 of Mukherjee, 2015), the Tso Morari Crystallines and the nearby regions (modified from Epard and Steck, 2008). The underlying topography map (90 m SRTM v4.1 DEM) was downloaded from USGS Earth Explorer website (<https://earthexplorer.usgs.gov/>) on July 2019. Earthquake data (accessed on 18 July 2017) as per USGS, Earthquake Hazards Program. OSS stands for Opposite Shear Sense. The cross-section presented below is along the X-Y line segment shown on the map.

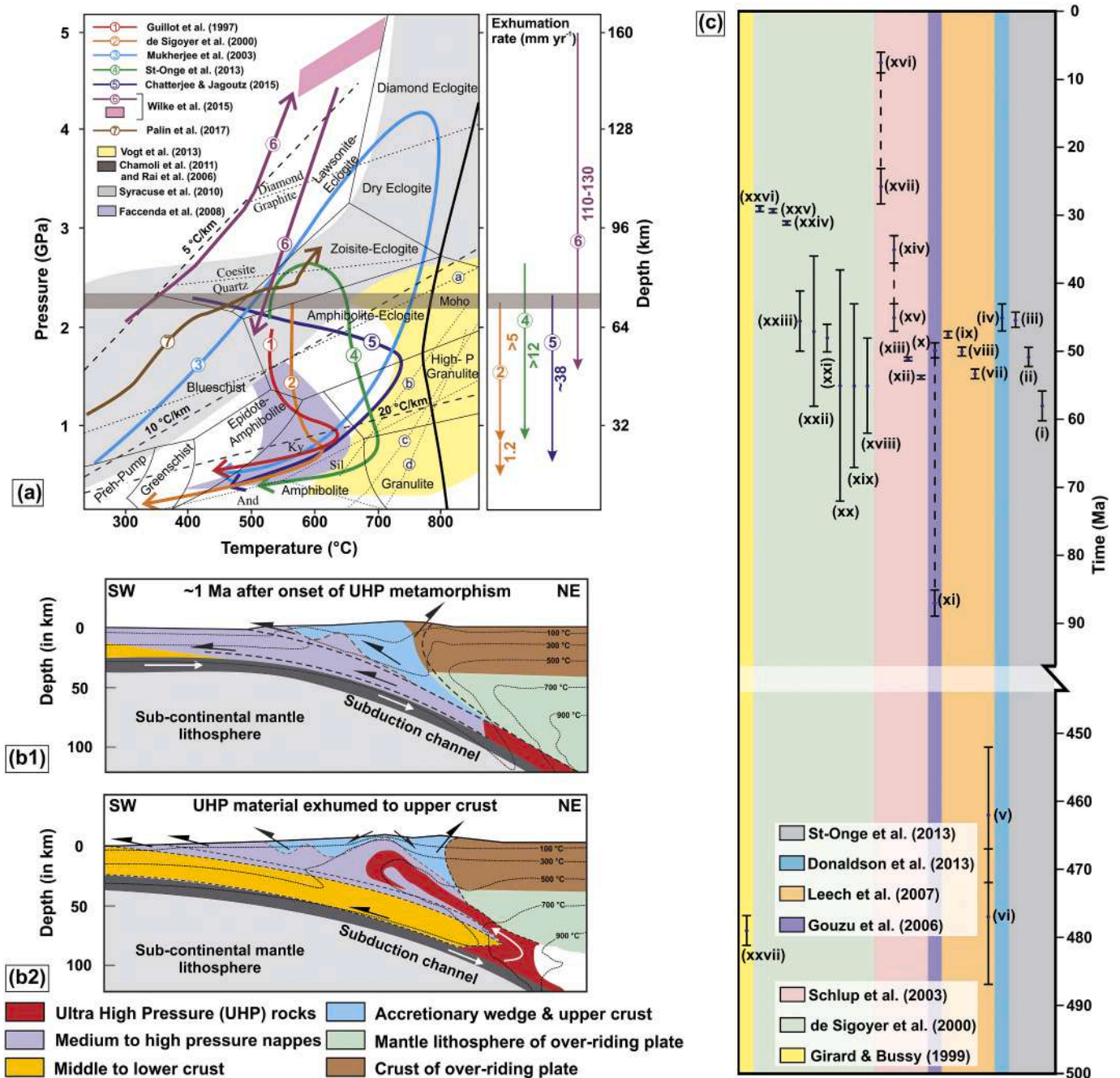


Fig. 2. (a) P-T paths of the host gneiss and eclogites of the TMC and the previously reported exhumation rates (compiled from Guillot et al. (1997), de Sigoyer et al. (2000), Mukherjee et al. (2003), St-Onge et al. (2013), Chatterjee and Jagoutz (2015) and Wilke et al. (2015); for details see Supplementary Table. S3). Syracuse et al. (2010) conducted 2-D numerical simulations to determine the P-T paths of the surfaces of subducting slabs. The results of the same are shown by the grey area. The purple and yellow regions represent the field of the numerically modelled P-T profiles of crustal slabs exhumed in a collisional belt (Faccenda et al., 2008) and oceanic subduction zones (Vogt et al., 2013), respectively. The brown zone shows the depth of the Moho in the region (Rai et al., 2006; Chamoli et al., 2011). Thick black solid line is the solidus for under-saturated continental crust (Auzanneau et al., 2006). Other reaction curves: (a) Jadeite + Quartz = Albite (Palin et al., 2017). (b) Dehydration melting curve of muscovite: Muscovite + Plagioclase + Quartz = Al₂SiO₅ + K-feldspar + melt (Labrousse et al., 2002). (c) Phengite breakdown: Phengite + Quartz = Al₂SiO₅ + K-feldspar + melt ± Biotite (Vielzeuf and Holloway, 1988). (d) Dehydration melting curve of biotite for a metapelite (Labrousse et al., 2002). The geothermal gradient curves and the facies grid are taken from Maruyama et al. (1996). Stability field curves for Kyanite (Ky)-Andalusite (And)-Sillimanite (Sil) are redrawn from Pattison (1992). The transition curves for coesite-quartz (Bohlen and Boettcher, 1982) and diamond-graphite (Bundy, 1980) are also shown. (b1,b2) Buoyancy driven 'pulse-like' exhumation of UHP crust in the form of a nappe stack from >100 km depth in a subduction channel underlying the accretionary wedge (reproduced from figs. 6 and A1 of Beaumont et al., 2009). (c) Absolute timing of the tectono-thermal events of the TMC (compiled from Girard and Bussy (1999), de Sigoyer et al. (2000), Schlup et al. (2003), Gouzu et al. (2006), Leech et al. (2007), Donaldson et al. (2013), and St-Onge et al. (2013); also see Supplementary Table. S4 for details). The error associated with each date are also shown. The dotted lines indicate the chronologic range of a single event. (For interpretation of the references to colour in this figure legend, the reader is referred to the web version of this article.)

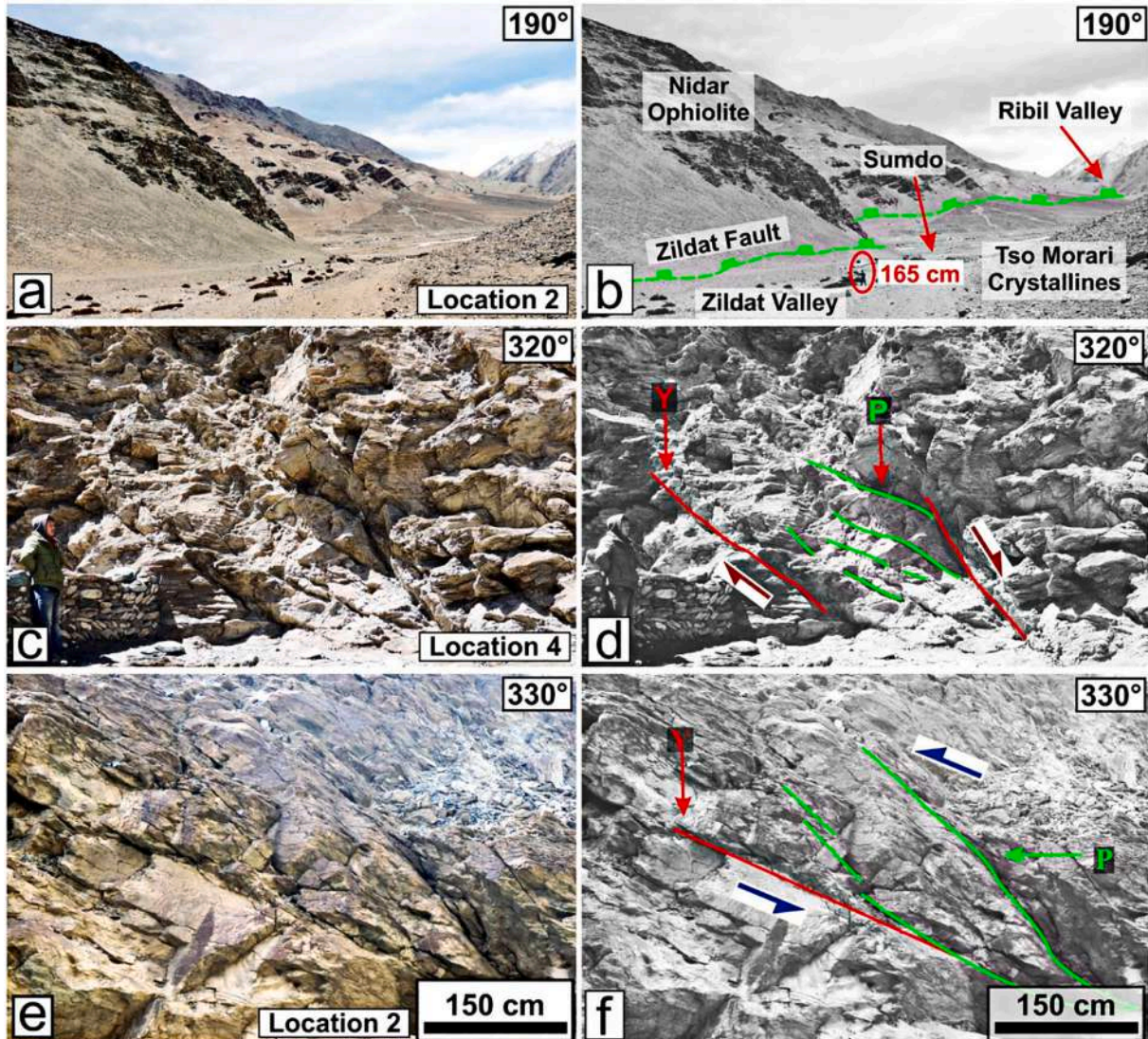


Fig. 3. Outcrop-scale kinematic indicators. (a,b) View from the Zildat Valley towards east showing the possible trace of the Zildat fault that separates the ophiolitic rocks from the TMC. (c,d) Top-down-to-N brittle shear sense (Y-plane, dip/dip direction: $55^{\circ}/280^{\circ}$). (e,f) Top-up-to-S brittle shear sense. The photo was clicked from a distance, hence orientation data unavailable. (g) Top-down-to-N ductile shear sense exhibited by a thin quartz vein (C-plane, dip/dip direction: $15^{\circ}/330^{\circ}$). (h) Sigmoid quartz clast (C-plane, dip/dip direction: $15^{\circ}/310^{\circ}$, S-plane, dip/dip direction: $25^{\circ}/125^{\circ}$) shows top-to-S ductile shear sense. (i) Top-up-to-N ductile shear sense (C-plane, dip/dip direction: $40^{\circ}/195^{\circ}$). (j) S-shaped, asymmetrically folded quartz vein displaying top-to-W ductile shear sense. Orientations of the stretching lineations (trend/plunge) have been written at the top right corner of (i) and (j). Stretching lineations could not be found at the rest of the locations presented here. (k) Stretching lineation on a hand specimen from the location 12 (Transect-A; Fig. 1). (l) Sketch of (k), with the foliation and lineation plotted on the stereonet. Figures (a) – (j) show vertical sections. (b), (d), (f) are the grayscale versions of (a), (c), (e), respectively. The azimuth direction corresponding to the right of each image is shown at the top-right corner of the respective image.

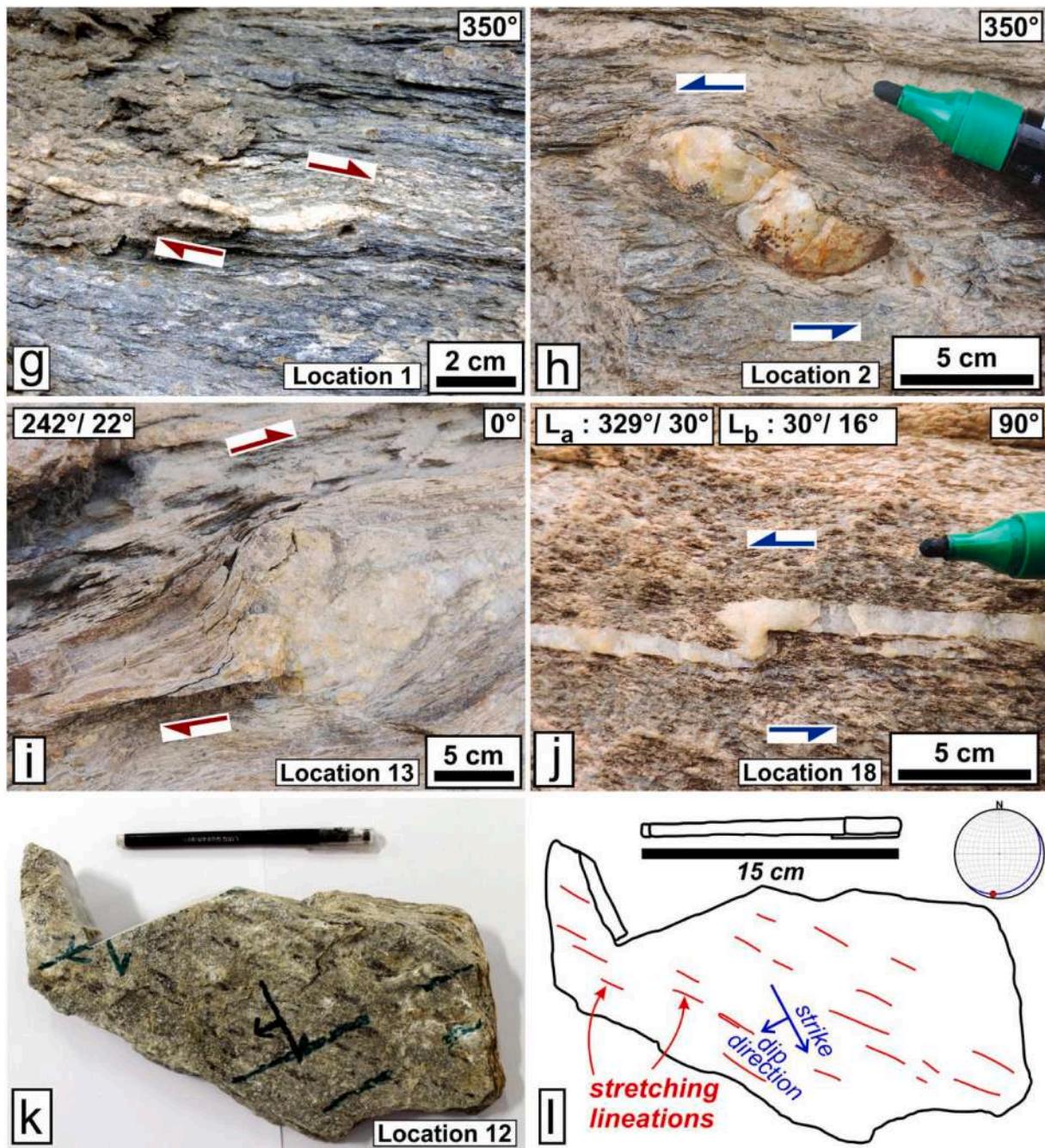


Fig. 3. (continued).

3.2. X-ray diffraction (XRD) analysis

The purpose of XRD analysis is to quantify the mineralogy of gneissic samples identified petrographically – particularly those in the vicinity of the ZSZ – and comment on the possibility of shear-induced enhanced fluid activity. Powdered samples (< 75 μm) are analyzed using the PANalytical Empyrean (PANalytical B.V., Almelo, The Netherlands) setup at the Department of Earth Sciences, IIT Bombay. The data thus obtained are interpreted using HighScore Plus software and the Inorganic Crystal Structure Database (ICSD).

3.2.1. Results

Quartz, potash and plagioclase feldspars, muscovite, and biotite are the major minerals present in the gneiss. The modal percentages of quartz and muscovite show a gradual rise towards the ZSZ (quartz

~36–56%, muscovite ~1–22%; over ~22 km) along both the transects (Fig. 4). However, an inverse relation is observed between the abundance of the feldspars and muscovite (Supplementary Fig. S5).

3.3. Microstructural study

3.3.1. Petrography

Twenty-five rock samples were collected from the field (locations in Fig. 1). We did not group the samples based on the stretching lineation owing to their varied trends. Instead, we classified the samples based on the presence/absence of stretching lineation. The samples are cut parallel to the stretching lineation and perpendicular to the foliation (XZ-sections), and are studied under an optical microscope. Two thin-sections are prepared from samples with two sets of stretching lineation (locations 6, 11, 16, 18, and 20 in Fig. 1). For the seven samples

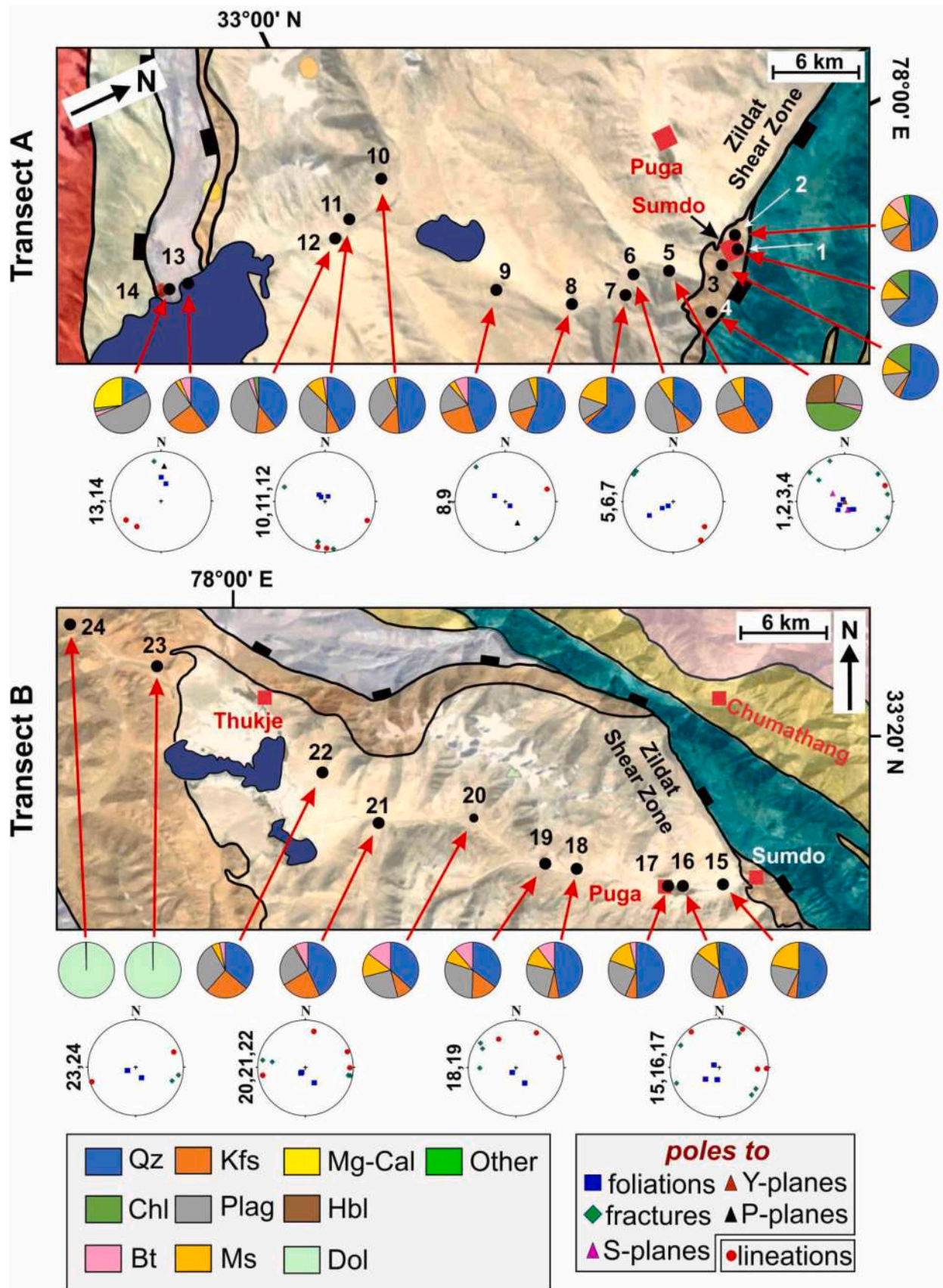


Fig. 4. Structural and mineralogical variations across the two transects A & B. The numbers beside the stereoplots represent the locations. Mineral abbreviations (in the grey box) are as per Whitney and Evans (2010).

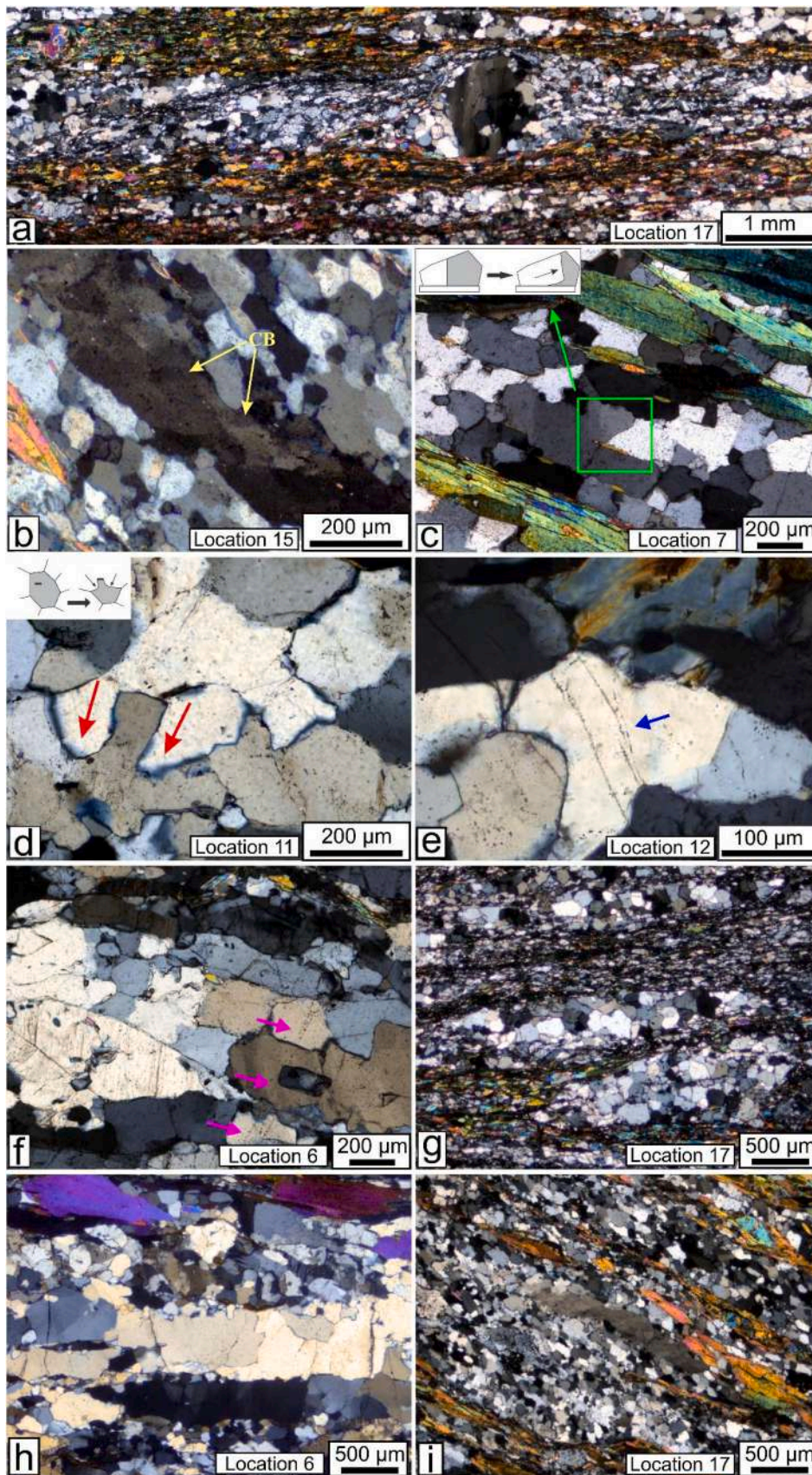
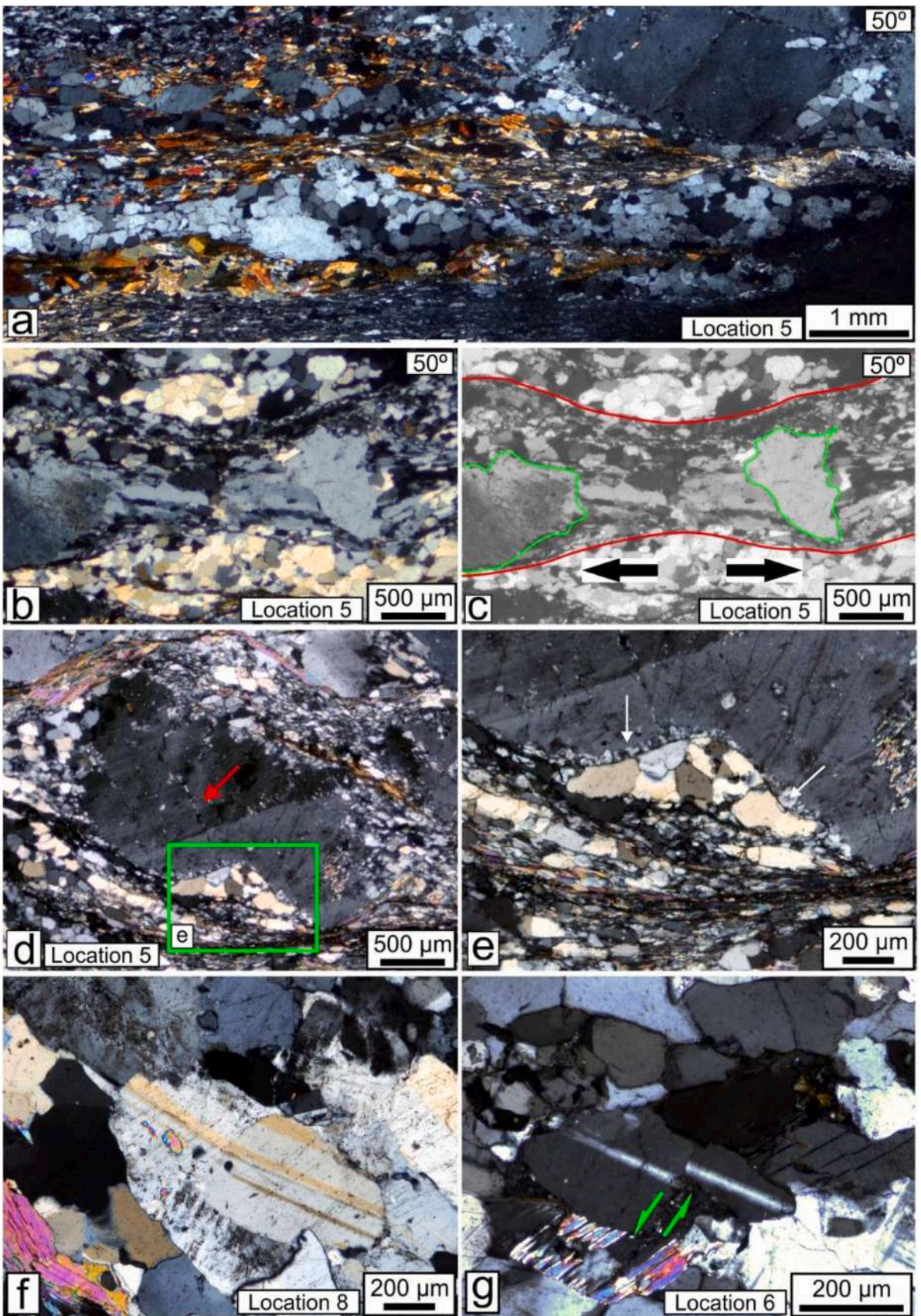


Fig. 5. Photomicrographs of the gneissic rocks showing the major deformation microstructures in quartz. (a) Core mantle structure of quartz. (b) Chessboard extinction (CB, pointed out with yellow arrow) in quartz. (c,d) Dragging microstructures (cartoon redrawn after [Passchier and Trouw, 2005](#)). Red arrows: direction of grain boundary migration. (e) Trails of secondary fluid inclusion within a single grain (blue arrow). (f) Linear trail of trans-crystal secondary fluid inclusions (pink arrows), near perpendicular to the quartz grain boundaries. (g) Grain-size variation of the quartz rich domains. Samples closer to the ZSZ exhibit such interconnected zones of finer grain size that are absent in samples farther away from the ZSZ (see (h)). (i) SGR recrystallization: Quartz ribbons surrounded by recrystallized grains of nearly same size as that of the subgrains. ([Stipp et al., 2002b](#)). Overall, the rocks exhibit a lepidoblastic texture. (For interpretation of the references to colour in this figure legend, the reader is referred to the web version of this article.)



(caption on next page)

Fig. 6. Deformation microstructures in quartz and feldspars. (a) Pinch and swell structure in mica rich and coarse-grained quartz domains. (b,c) Neck fold in between boudinaged K-feldspar porphyroclasts (bounded by green curves). Red curves indicate the boundaries of the boudinaged structures. The thick arrows indicate foliation parallel extension direction. (d,e) Core-mantle structures in K-feldspar. Thin mantle of recrystallized grains surround the porphyroclasts. The porphyroclasts also consist of thin, linear bands of fine grains (red arrow), which may have recrystallized along intra-granular fractures (acute angles between the fractures and the C-plane ranges $\sim 5\text{--}50^\circ$). It is likely that the recrystallisation of grains was synchronous with brittle fracturing ($< 450^\circ\text{C}$; Passchier and Trouw (2005)). (e) Enlarged view of the part of (d) demarcated with the GREEN box. White arrows point to the sharp boundary between the mantle of the porphyroblast and surrounding quartz grains of the matrix. (f) Distorted twin lamellae possibly due to subgrain formation. (g) Displaced twin lamellae in plagioclase indicating intra-granular micro-fault. The azimuth directions corresponding to the right of images (a), (b), and (c) are shown at the top-right corner of the respective photomicrographs. (For interpretation of the references to colour in this figure legend, the reader is referred to the web version of this article.)

devoid of prominent lineation (locations 1, 3, 5, 7, 8 and 10 in Fig. 1), sections are cut parallel to the dip direction (Supplementary Fig. S4). This is a standard process of obtaining oriented thin-sections of such rocks (e.g., Long et al., 2011). Recently, Bose and Gupta (2020) proposed that the development of stretching lineations in quartzo-feldspathic rocks depends on both shearing temperature and strain rate.

The quartzo-feldspathic gneiss also contains garnet, mostly euhedral and a few skeletal/relict (Supplementary S.1). Calcareous meta-sedimentary rocks with minor amounts of plagioclase feldspar occur near the western border of the TMC (locations 23 and 24) (Fig. 4).

3.3.2. Quartz deformation microstructures

Quartz is the most dominant mineral in the samples. Its proportion increases gradually towards the ZSZ along both the transects (Fig. 4). The grains are subidioblastic to xenoblastic. Deformation temperatures are estimated based on the recrystallisation mechanisms (Stipp et al., 2002a, 2002b). This fabric-based deformation thermometer holds for natural strain rates ($10^{-14\pm 1}\text{ s}^{-1}$; review in Bose and Mukherjee, 2020) and water-deficient conditions (H content in quartz grains < 2000 ppm; Kronenberg et al., 1990). Whereas the strain rate values for the TMC are unavailable, the granitic protolith was anhydrous (Palin et al., 2017). Palin et al. (2014) based on metamorphic studies, reported dehydration of the Tso Moriri gneiss at 7–9 kbar and $\sim 610\text{--}725^\circ\text{C}$ during extrusion.

Asymmetric core-mantle structures in quartz are present (Fig. 5a). Subgrains inside the core clearly demonstrate deformation in SGR to SGR-GBM transition regime i.e. $400\text{--}500^\circ\text{C}$ (Stipp et al., 2002a, 2002b). Chessboard extinction, indicative of $> 700^\circ\text{C}$ (Stipp et al., 2002a, 2002b), is noted in the relict grains (Fig. 5b, Supplementary Fig. S8). Dragging microstructures (Fig. 5c,d) suggesting grain boundary migration (GBM) recrystallisation ($550\text{--}700^\circ\text{C}$, Stipp et al., 2002a, 2002b) are also present.

Both intra- and trans-granular fluid inclusions exist (Fig. 5e,f) ($< 300^\circ\text{C}$, Vernon, 2018). Sizes of quartz grains, measured from the monomineralic ribbons (Supplementary Figs. S6–S7) are moderate (Feret diameter: $200\text{--}600\ \mu\text{m}$) to coarse (Feret diameter: $> 600\ \mu\text{m}$) throughout, with domains of finer grains in between (Fig. 5). The thickness and the frequency of such fine-grained domains increase towards the ZSZ (compare Fig. 5g and h) along with the muscovite content. However, we cannot comment whether these two features are interdependent. These fine-grained domains contain coarser quartz grains (long axis: $\sim 1200\ \mu\text{m}$) with subgrains of sizes comparable to the surrounding grains (Fig. 5i). These indicate subgrain rotation (SGR) recrystallisation mechanism. Pinch and swell structures (Fig. 6a,b) suggest foliation-parallel extension.

3.3.3. Feldspar deformation microstructures

Most of the moderate- to coarse-grained (mostly subidioblastic) feldspars (especially K-feldspars), from both the transects (A and B) are fractured. A thin layer of recrystallized grains exists along the rims of some K-feldspar porphyroclasts that act as cores (Fig. 6d). This mantle shares a sharp boundary with the core and the surrounding quartz-rich layer (Fig. 6e), and denotes deformation within $450\text{--}600^\circ\text{C}$ (Passchier and Trouw, 2005). Plagioclase with bent twin planes (Fig. 6f) and micro-faults (Fig. 6g) are also present and indicate intracrystalline deformation

under a low metamorphic grade ($< 400^\circ\text{C}$) (Passchier and Trouw, 2005).

3.3.4. Opposite shear senses

Twenty-seven thin-sections are studied under an optical microscope to note the presence of opposite shear senses (OSS; general review in Dutta and Mukherjee, 2019). Hippert and Tohver (1999) use the term “reverse shear” for such structures and described them as, any movement along the main shear zone boundary (shear plane) opposite to the overall shear sense displayed by the rock. Fourteen thin-sections (from both the transects A & B) show prominent OSS, wherein one sense outnumbers the other. A sample from location 20 (Transect-B) (Fig. 1) is of particular importance, since both shear senses are almost equally numerous. The rest of the thirteen thin-sections do not exhibit OSS. Higher number of stretching lineations plunge easterly and northeasterly, thus top-down-to-NE/E is the dominant shear sense observed. Several examples are presented in Fig. 7, some of which exhibit OSS even in individual photomicrographs (Fig. 7a–f). In other cases, two different images from a single thin section are presented, each displaying a different shear sense (Fig. 7g–j). No cross-cut relation has been noticed between any of the shear planes.

3.4. Quartz grain statistics

We measured several parameters viz., Feret Diameter (diameter of the circle with equivalent area), aspect ratio (length of axis to that of the short axis), and vector mean strength (\bar{a}) (eq. 1) (Cladouhos, 1999; Menegon et al., 2008) from recrystallized quartz grains to assess the variation in deformation intensity of the gneiss across the TMC. Grain boundary lobateness (using PARIS factor of Panozzo and Hurlimann, 1983) is measured as a proxy to deformation temperature – higher temperature produces grains with greater lobateness (Stipp et al., 2002a, 2002b). Finally, the mean values of all these parameters are calculated for each thin-section and are utilized for subsequent interpretations.

In the formula (Menegon et al., 2008),

$$\bar{a} = \left[\frac{(\sum \sin 2\theta)^2 + (\sum \cos 2\theta)^2}{N} \right]^{1/2} \quad (1)$$

\bar{a} is the vector mean strength, θ is the angle between the long axis of the quartz grain and the macroscopic foliation (measured anticlockwise), and N is the total number of quartz grains (in the scanned area). Grains with aspect ratios > 1.3 are considered (as per Cladouhos, 1999). \bar{a} varies from 0 (undeformed rocks) to 1 (highly deformed rocks) (see Menegon et al., 2008).

At least 300 quartz grains are chosen from each thin-section to ensure reliable statistical results. All measurements are made on the XZ-sections of the samples (sections parallel to the dip direction were cut from samples without prominent lineations; Section 3.3.1). Samples from location 6 and 10 (Transect-A), and 16, 18 and 20 (Transect-B; Fig. 1) show two sets of stretching lineations (L_a : more prominent; L_b : less prominent, Supplementary Fig. S4), hence, two different thin-sections are prepared and studied.

Secondary/relatively weaker minerals in rocks e.g., feldspar and mica tend to absorb most of the strain, thereby hindering quartz to

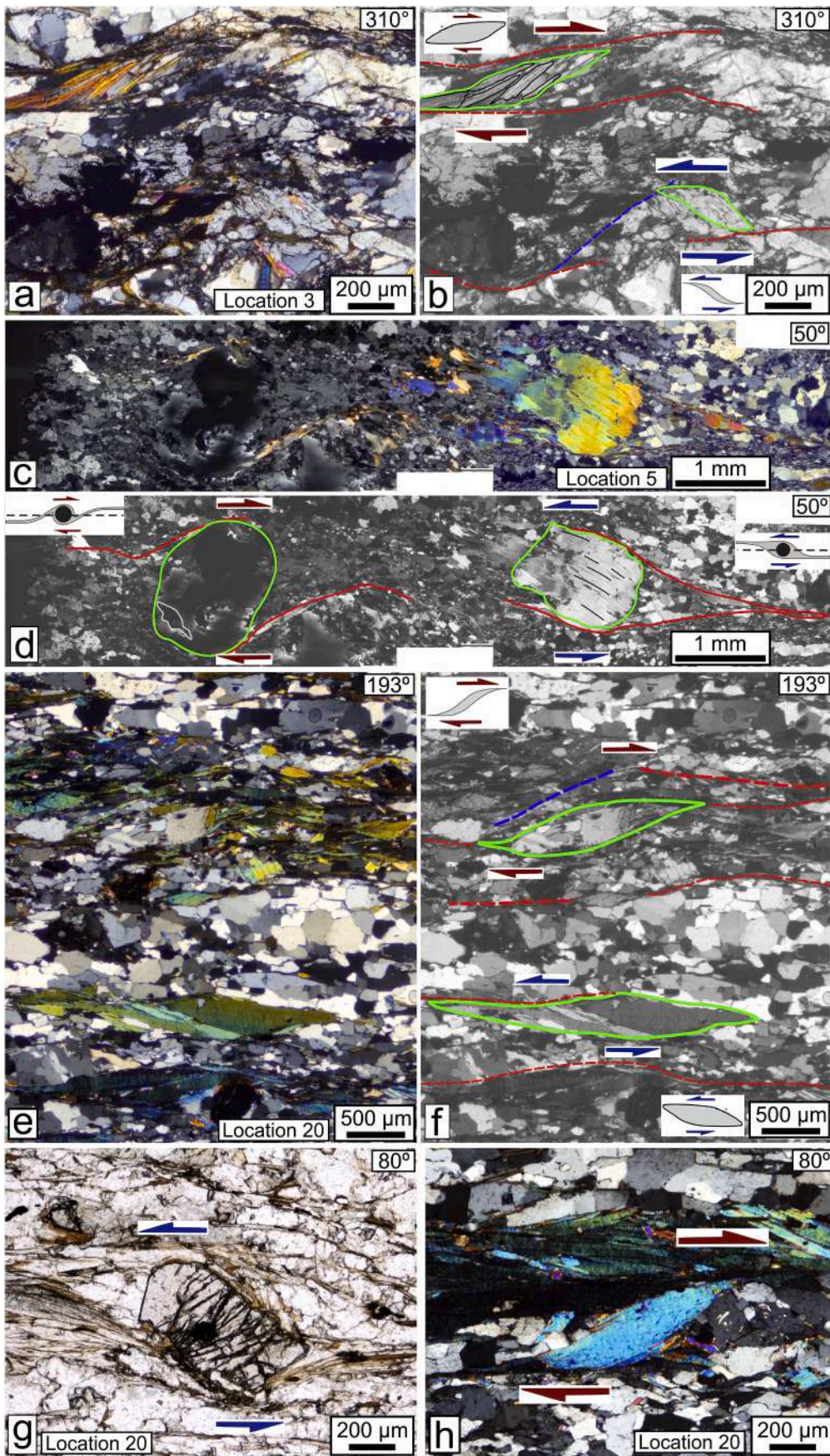


Fig. 7. Opposite shear senses. (a,b) The muscovite aggregate (type 2a1 mineral fish; Mukherjee, 2011) shows top-to-NW shear and the K-feldspar fish (type 1a1 mineral fish; Mukherjee, 2011) below displays top-to-SE shear (cartoon diagram redrawn after . figs. 5.20 & 5.28a of Passchier and Trouw (2005)). (c,d) Top-to-NE and top-to-SW shear senses shown by the δ -type mantled porphyroclast (K-feldspar) to the left, and the σ_a -type mantled porphyroclast (muscovite) to the right, respectively. It is to be noted that the fine-grained tail to the left, for the σ_a -type porphyroclast, has developed partially (cartoon diagrams redrawn after . fig. 5.20 of Passchier and Trouw (2005)). Rotations of minerals depend upon the type of flow as well as the pre-deformational orientation of the minerals and back-rotated clasts are common. But, back-rotated clasts typically display shadows/tails indicating forward shearing (see fig. 8a by Xypolias, 2010). (e,f) An aggregate of quartz-feldspar-muscovite with top-S shear sense (blue dashed curve: S-plane.). Below, the muscovite fish shows top-to-N shear. The fish appears to be an aggregate of several muscovite grains (cartoon diagram redrawn after . figs. 5.20 & 5.28a of Passchier and Trouw (2005)). The quartz-rich domain above the muscovite fish shows a hypidioblastic texture. (g) Top-to-W shear exhibited by σ_a -type mantled garnet porphyroblast (cartoon diagram redrawn after . fig. 5.21 of Passchier and Trouw (2005)). Fractures inside garnet grain are near perpendicular to the S-plane. (h) Top-to-E shear. Red dashed curves: foliation or C-planes. The grains considered as kinematic indicators are marked with green curves. (b), (d), (f) are the grayscale versions of (a), (c), (e), respectively. The azimuth directions corresponding to the right of each image is shown at the top-right corner of the respective photomicrograph. (For interpretation of the references to colour in this figure legend, the reader is referred to the web version of this article.)

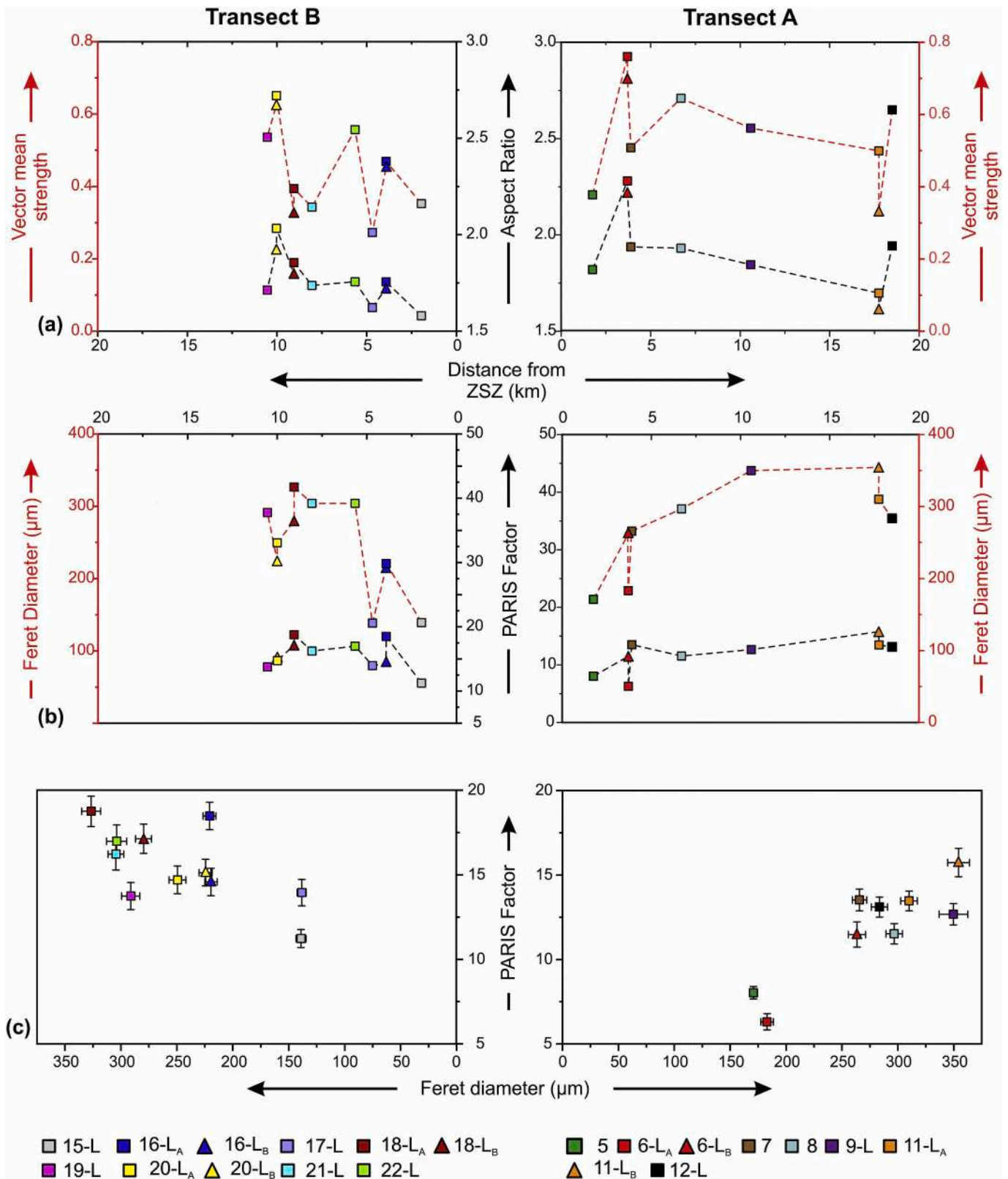


Fig. 8. Quartz grain parameters. Variation of (a) aspect ratio & vector mean strength and (b) PARIS factor & Feret Diameter away from the ZSZ along the two transects. The colours of the dashed lines correspond to that of the Y-axes in (a) and (b). (c) Plot showing variation of the Feret Diameter with the PARIS factor. The colored See Fig. 1 for sample locations.

Table 2
Grain parameters measured from recrystallized quartz grains in monocrystalline ribbons. For the locations see Fig. 1.

Sample	Mean Feret Diameter ^a (error)(μm)	Mean aspect ratio ^b (error)	Mean PARIS factor ^c (error)	Vector mean strength ^d	Total number of grains
Transect A					
5	170.87 (\pm 3.60)	1.82 (\pm 0.13)	8.03 (\pm 0.37)	0.38	508
6-1 _a	182.95 (\pm 5.68)	2.28 (\pm 0.08)	6.31 (\pm 0.48)	0.76	406
6-1 _b	263.40 (\pm 7.66)	2.22 (\pm 0.09)	11.48 (\pm 0.74)	0.70	376
7	265.73 (\pm 6.41)	1.94 (\pm 0.20)	13.52 (\pm 0.64)	0.51	456
8	296.73 (\pm 7.40)	1.93 (\pm 0.04)	11.52 (\pm 0.60)	0.64	379
9	349.69 (\pm 12.84)	1.84 (\pm 0.03)	12.68 (\pm 0.63)	0.56	410
11-1 _a	310.00 (\pm 7.46)	1.70 (\pm 0.04)	13.47 (\pm 0.58)	0.50	452
11-1 _b	354.35 (\pm 9.78)	1.62 (\pm 0.02)	15.74 (\pm 0.84)	0.33	407
12	283.57 (\pm 7.28)	1.94 (\pm 0.06)	13.10 (\pm 0.60)	0.61	427
Transect B					
15	139.01 (\pm 4.47)	1.58 (\pm 0.02)	11.22 (\pm 0.53)	0.35	369
16-1 _a	220.79 (\pm 5.73)	1.75 (\pm 0.04)	18.48 (\pm 0.81)	0.47	381
16-1 _b	219.47 (\pm 5.62)	1.72 (\pm 0.03)	14.57 (\pm 0.81)	0.46	408
17	138.42 (\pm 4.00)	1.62 (\pm 0.07)	13.94 (\pm 0.78)	0.27	304
18-1 _a	326.57 (\pm 8.43)	1.86 (\pm 0.15)	18.75 (\pm 0.90)	0.39	382
18-1 _b	279.71 (\pm 7.08)	1.80 (\pm 0.18)	17.13 (\pm 0.87)	0.33	408
19	291.20 (\pm 8.15)	1.71 (\pm 0.04)	13.74 (\pm 0.80)	0.54	314
20-1 _a	249.42 (\pm 7.50)	2.03 (\pm 0.04)	14.70 (\pm 0.82)	0.63	400
20-1 _b	224.32 (\pm 5.78)	1.92 (\pm 0.03)	15.12 (\pm 0.79)	0.65	514
21	303.80 (\pm 8.95)	1.76 (\pm 0.03)	16.98 (\pm 0.97)	0.56	356
22	304.47 (\pm 7.06)	1.74 (\pm 0.05)	16.22 (\pm 0.94)	0.34	326

Note: a: diameter of the circle with equivalent area; b: ratio of long axis to the short axis; c: Panozzo and Hurlimann (1983); d: Cladouhos, 1999; Menegon et al., 2008.

deform (Hunter et al., 2019; Graziani et al., 2020). Consequently, these measurements have mostly been performed on quartzites (Heilbronner and Kilian, 2017; Hunter et al., 2018a) with minimal (<10% by vol.) secondary minerals. However, since polymineralic rocks are more abundant at some terranes than pure quartzites, quartz grains from such samples can not be completely overlooked/avoided in kinematic investigations (e.g. Fazio et al., 2017; Puelles et al., 2018). Therefore, we measure the grains only from the monomineralic quartz ribbons with no/minimal weaker phases in the vicinity (at least 20 μm). Such ribbons have also been used in previous studies (Palazzin et al., 2016; Hawemann et al., 2019) from polymineralic rocks. The grains from the photomicrographs are manually digitised in QGIS 3.4 (2018) (Supplementary Fig. S6). The shapefiles, thus obtained, are fed into MATLAB (R2018a), and analyzed with the PolyLx (version R3.1, 2015) (<https://petrol.natur.cuni.cz/~ondro>).

3.4.1. Results

The aspect ratios of the quartz grains decrease steadily away from ZSZ for Transect-A (1.8 to 1.6 over \sim 18 km), whereas the data from Transect-B shows a zig-zag pattern (black dashed lines in Fig. 8a). The ranges for transects A and B are 1.68–2.28 and 1.58–2.03, respectively. Interestingly, the pattern of variation displayed by the vector mean strength (Fig. 8) along both the transects match almost exactly with that of the aspect ratio. For both the transects, the Feret diameters drop close to the ZSZ (red dashed lines in Fig. 8b,c; Table 2; Supplementary Fig. S7). All these observations reflect the expected increase in shear deformation near the ZSZ. The PARIS factor variations across the transects are minimal (Fig. 8b,c). Higher PARIS factors for Transect-B than Transect-A imply that the grains are more lobate and hence signify higher deformation temperatures.

3.5. Electron backscatter diffraction

The crystallographic directions of the constituent minerals of a deformed rock usually systematically arrange the crystal lattice, which is called the Crystallographic Preferred Orientation (CPO) (Schmid and Casey, 1986). Depending upon the strain path/kinematic history, quartz \langle c \rangle -axis pole figures can either be symmetric (coaxial deformation) or asymmetric (non-coaxial deformation) (Passchier and Trouw, 2005). The latter can be used to infer shear senses (e.g. Bouchez et al., 1983; Kilian et al., 2011 etc.), which must be cross-checked with other shear sense indicators as well (Dutta and Mukherjee, 2019). The CPO pattern can also aid in constraining the deformation temperature (Fig. 9) (review in Law, 2014).

3.5.1. Quartz CPO and misorientation analyses

The one-point per grain pole figures (Figs. 10–12; Supplementary Figs. S10–S19) are calculated with de la Vallée Pousin kernel, halfwidth of 10° using MTEX 5.2.2 (Hielscher and Schaeben, 2008), and plotted on the kinematic reference frame (KRF) i.e. the vorticity normal section (VNS; Sec. 3.5.2). Samples with prominent stretching lineations (A: locations 6, 9, and 11; B: locations 15, 16, 18, 19, 20, 21, and 22) on them are only considered for this study. Samples from location 6, 10, 16, 18, and 20 (Fig. 1) show two sets of stretching lineations (L_a : more prominent; L_b : less prominent, Supplementary Fig. S4), hence, two different thin-sections are prepared and studied.

The point (P), girdle (G), and random (R) shape indices (Vollmer, 1990) of crystal axes distributions are computed for each pole figure. The magnitudes of P, G and R (Table 3; P + G + R = 1) display how well the \langle c \rangle -axis plots exhibit a point, a girdle, or a random distribution. The magnitude of R decreases with increase in sharpness of the CPO plot and vice-versa. Other CPO strength indices viz., the texture index (J) (Bunge, 1982), the entropy index (E) (Schaeben, 1988), and the misorientation index (M) (Skemer et al., 2005) are determined as well.

The opening angles (OA), angle of obliquity (α) and symmetry value (S) for the individual \langle c \rangle -axis pole figures are also determined using the

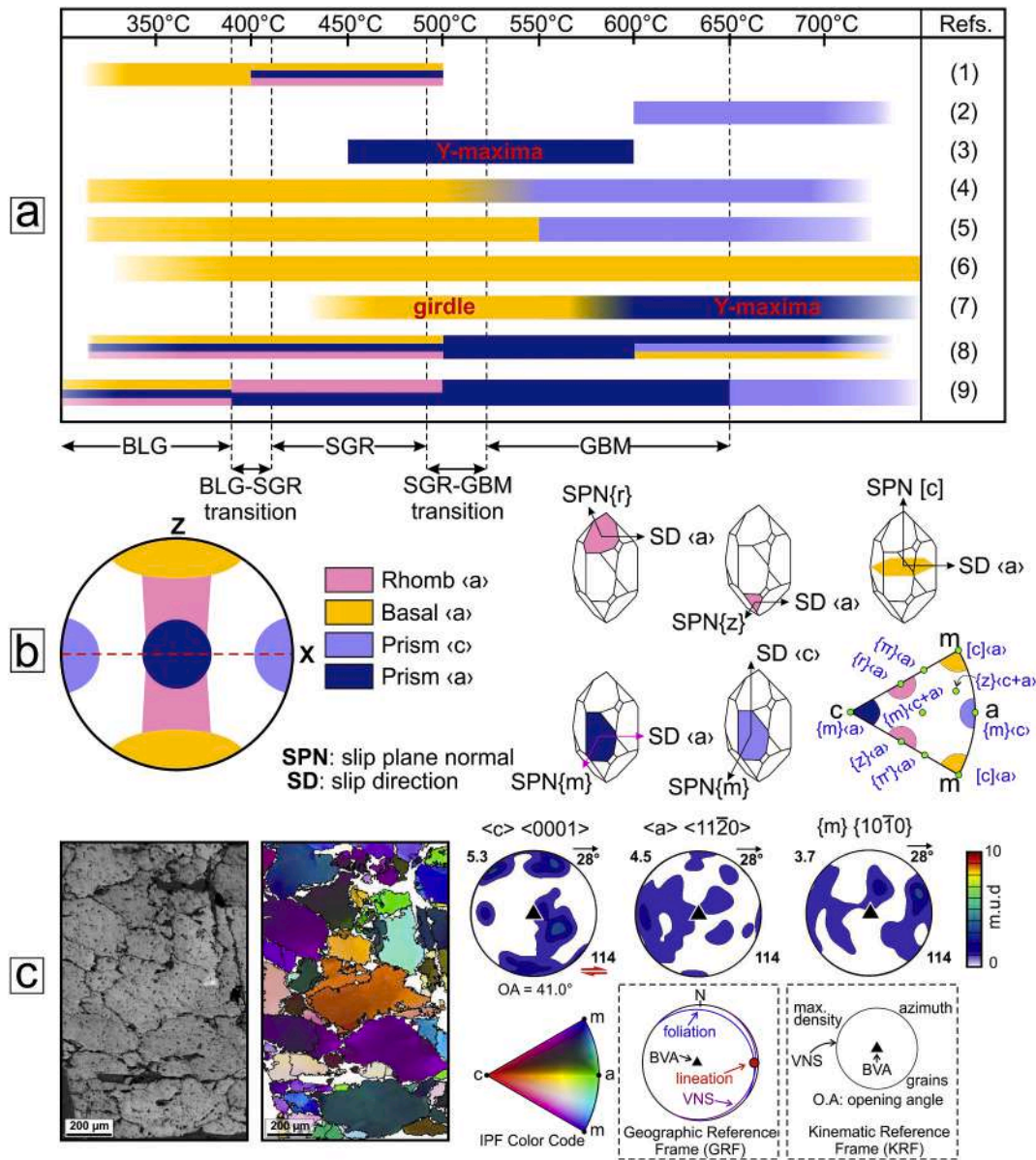


Fig. 9. (a) Slip systems and the corresponding ranges of deformation temperatures. (1) Baëta and Ashbee (1969), (2) Mainprice et al. (1986), (3) Schmid and Casey (1986), (4) Okudaira et al. (1995), (5) Takeshita (1996), (6) Kruhl (1998), (7) Kurz et al. (2002), (8) Stipp et al. (2002b), and (9) Passchier and Trouw (2005) (modified from Toy et al., 2008; references (1), (8) and (9) are our addition). More than one colour (one above another) indicates coeval activity of different slip systems. Faded portions denote uncertainty of continuity of the slip system. Temperature range of the dominant quartz recrystallization mechanisms are also marked (Stipp et al., 2002b). (b) Possible slip systems and the corresponding locations of (c)-axis maxima in the pole figure (modified after Schmid and Casey, 1986). Slip planes and directions of the most common slip systems in quartz (modified after Neumann, 2000). The colors correspond to the slip systems mentioned in (b). (c) Back-scattered electron (BSE) image from the thin-section (location 22, Fig. 1) and the corresponding colour coded EBSD map. The lower hemisphere, equal area pole figure plots of the (left to right) (c)- and (a)- axes, and poles to the {m}-planes are also shown. The pole figures are contoured to multiples of uniform density (m.u.d), and plotted on a kinematic reference frame (KRF; also see the legend below to interpret the numbers). The orientations of the foliation (blue girdle), lineation (red circle), vorticity normal section (purple girdle) and the bulk vorticity axis (BVA, black triangle) in a geographic reference frame (GRF) for the corresponding location are also displayed in the stereoplot below. (For interpretation of the references to colour in this figure legend, the reader is referred to the web version of this article.)

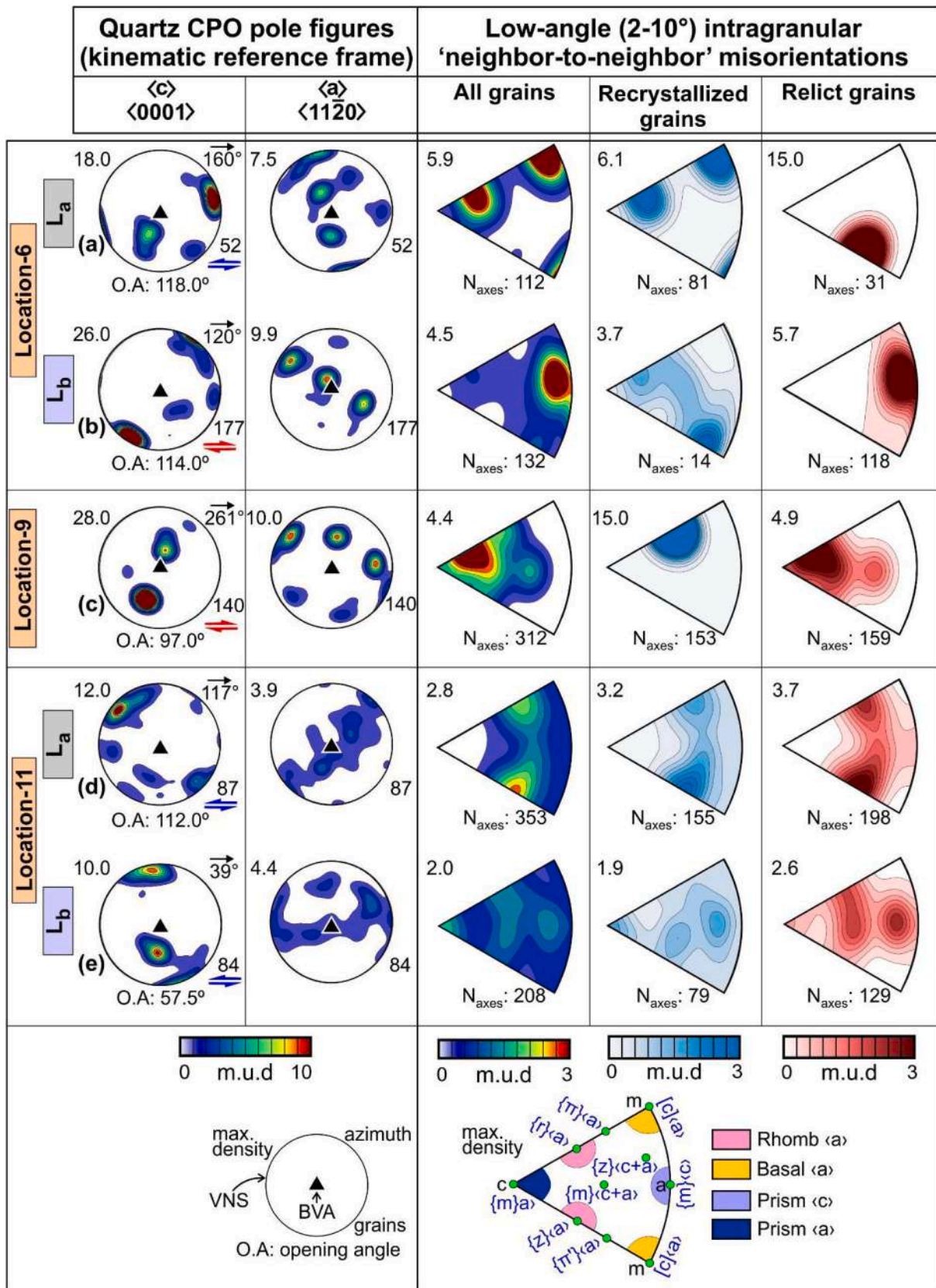


Fig. 10. Selected results of quartz CPO and low angle (2-10°) intragranular 'neighbor to neighbor' misorientation analyses for locations 6, 9 and 11. The lower hemisphere, equal area pole figures for the (left to right) $\langle c \rangle$ -, $\langle a \rangle$ - axes are contoured to multiples of uniform density (m.u.d), and plotted on a kinematic reference frame (KRF) such that the bulk vorticity axis (BVA) lies at the centre (as shown below). The inverse pole figures show the distribution of low angle (2-10°) misorientation axes, and are also contoured to m.u.d. The inverse pole figure to the bottom right (redrawn after Neumann, 2000) present the distribution of misorientation axes for the most common slip-systems in quartz.

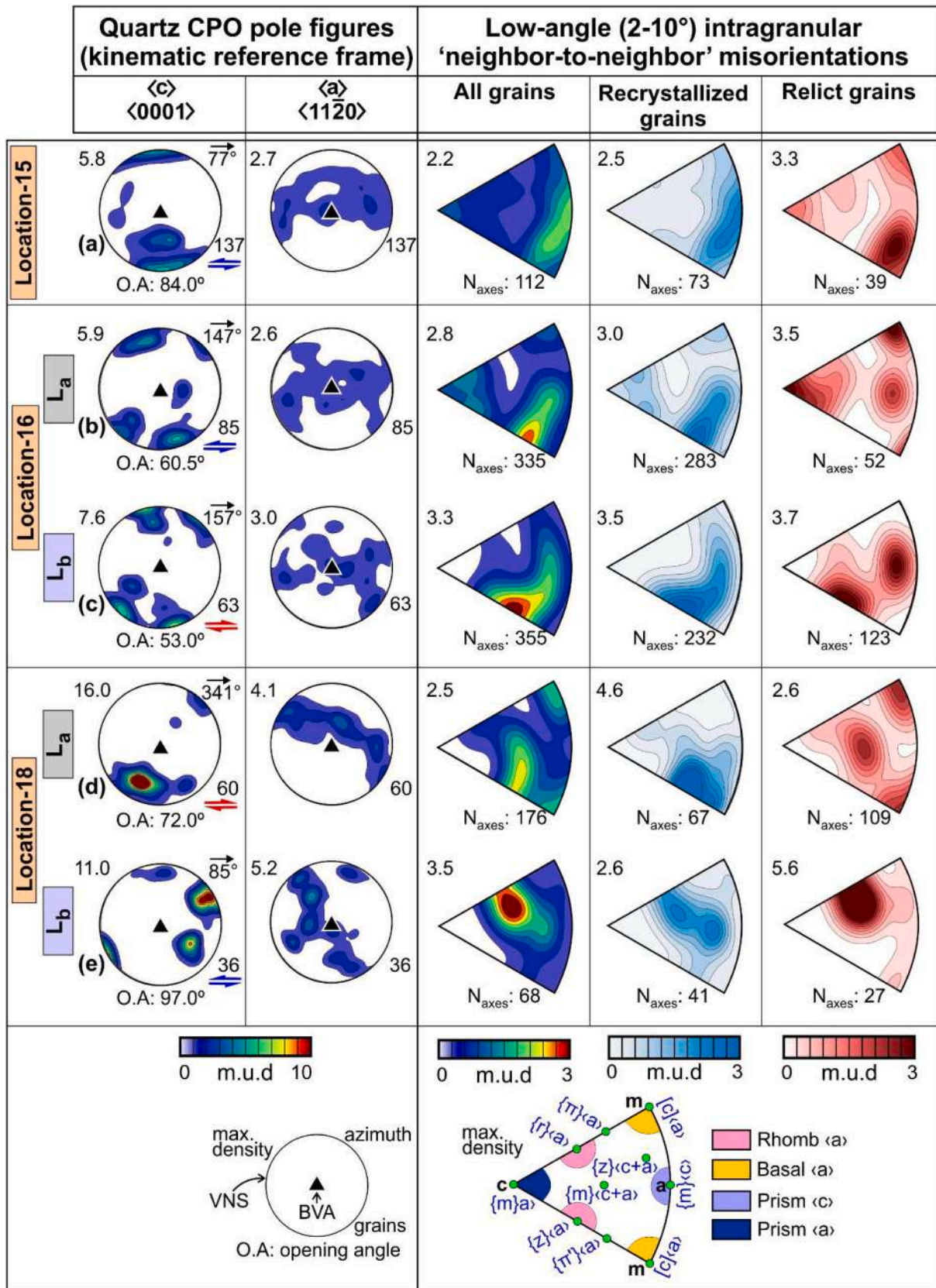


Fig. 11. Selected results of quartz CPO and low angle (2–10°) intragranular 'neighbor to neighbor' misorientation analyses for locations 15, 16 and 18. The lower hemisphere, equal area pole figures for the (left to right) $\langle c \rangle$ -, $\langle a \rangle$ - axes are contoured to multiples of uniform density (m.u.d), and plotted on a kinematic reference frame (KRF) such that the bulk vorticity axis (BVA) lies at the centre (as shown below). The inverse pole figures show the distribution of low angle (2–10°) misorientation axes, and are also contoured to m.u.d. The inverse pole figure to the bottom right (redrawn after Neumann, 2000) present the distribution of misorientation axes for the most common slip-systems in quartz.

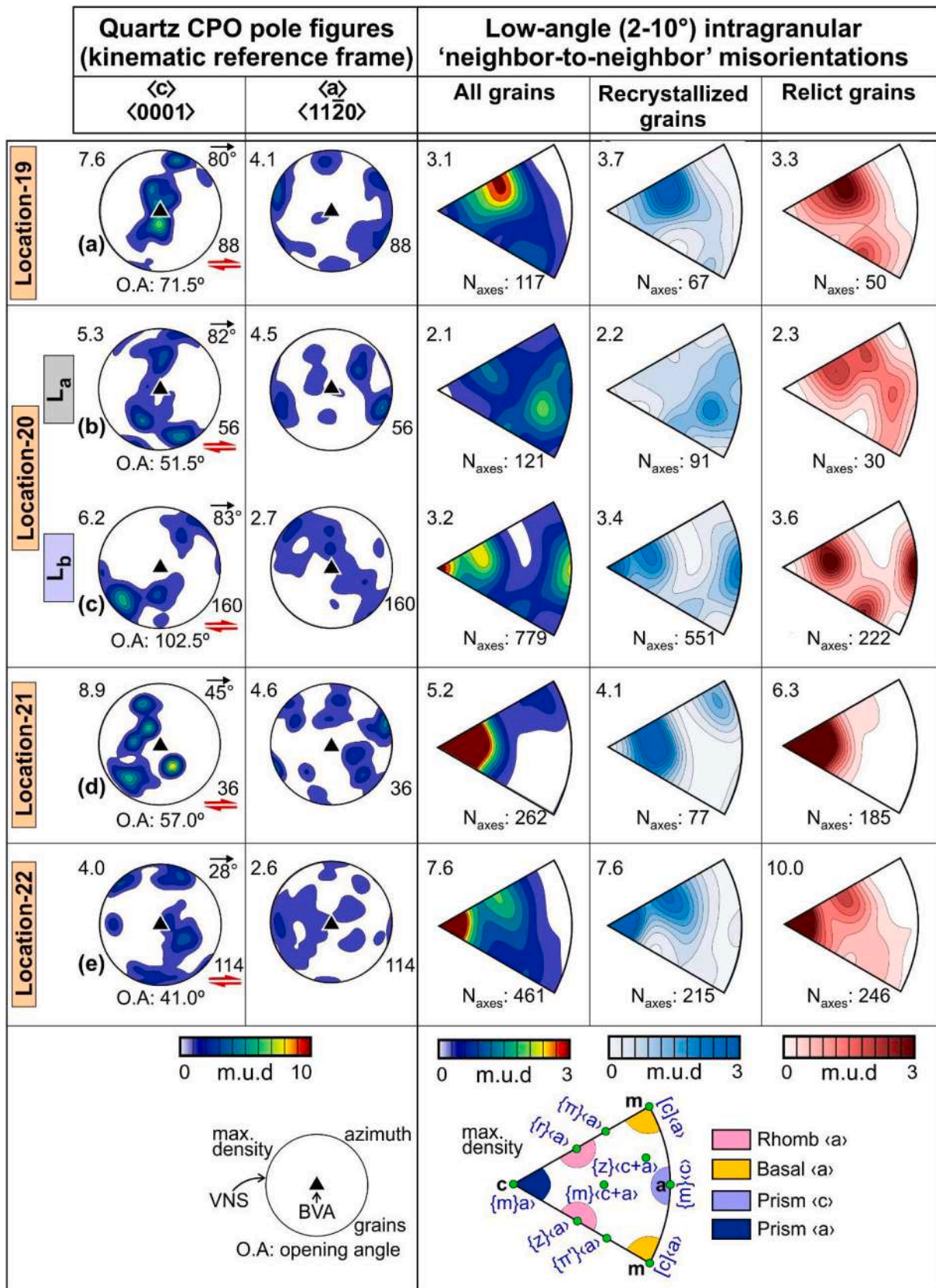


Fig. 12. Selected results of quartz CPO and low angle (2–10°) intragranular ‘neighbor to neighbor’ misorientation analyses for locations 19, 20, 21 and 22. The lower hemisphere, equal area pole figures for the (left to right) $\langle c \rangle$ -, $\langle a \rangle$ - axes are contoured to multiples of uniform density (m.u.d), and plotted on a kinematic reference frame (KRF) such that the bulk vorticity axis (BVA) lies at the centre (as shown below). The inverse pole figures show the distribution of low angle (2–10°) misorientation axes, and are also contoured to m.u.d. The inverse pole figure to the bottom right (redrawn after Neumann, 2000) present the distribution of misorientation axes for the most common slip-systems in quartz.

Table 3

Pole figure intensities and other strength parameters. For the locations see Fig. 1. Figure numbers starting with S refer to Supplementary Figures (S10-S19).

Sample	Scan no.	CPO Strength Indices ^a			ODF Parameters ^b			Pole Figure Intensity - J Index ^c	
		P	G	B	M	J	E	<c> <0001>	<a> <11-20>
6-L _a	S10a	0.1	0.5	0.6	0.1	5.4	-1.2	3.1	1.6
	S10b	0.3	0.3	0.6	0.1	7.1	-1.4	3.7	2.0
	S10c	0.3	0.1	0.4	0.1	6.5	-1.4	2.9	2.1
	10a	0.3	0.5	0.8	0.1	12.6	-1.8	6.0	2.9
6-L _b	10b	0.6	0.3	0.9	0.3	17.6	-2.0	8.6	3.7
	S10d	0.7	0.1	0.8	0.4	11.4	-1.9	6.2	2.5
	S10e	0.1	0.7	0.8	0.1	7.6	-1.4	3.7	2.2
9	S11a	0.2	0.2	0.4	0.1	4.1	-1.0	2.4	1.5
	S11b	0.3	0.5	0.8	0.1	13.9	-1.8	5.7	3.0
	10c	0.4	0.5	0.9	0.3	29.9	-2.6	10.6	5.5
11-L _a	S11c	0.3	0.2	0.5	0.1	4.2	-1.0	2.6	1.5
	S11d	0.3	0.3	0.6	0.1	5.3	-1.2	2.7	1.8
	10d	0.4	0.4	0.8	0.2	5.4	-1.2	3.3	1.7
11-L _b	S11e	0.3	0.3	0.6	0.1	4.3	-1.0	2.8	1.5
	10e	0.4	0.4	0.8	0.2	6.1	-1.4	4.4	1.8
	S12a	0.4	0.4	0.8	0.2	5.8	-1.3	3.4	1.8
15	S12b	0.5	0.3	0.8	0.2	6.4	-1.4	3.1	2.1
	11a	0.4	0.3	0.7	0.2	3.6	-1.0	2.6	1.5
16-L _a	S12c	0.1	0.6	0.7	0.1	9.8	-1.8	3.8	2.3
	S12d	0.3	0.1	0.4	0.1	4.5	-1.0	2.7	1.6
	S12e	0.1	0.5	0.6	0.1	4.6	-1.2	2.6	1.5
	S13a	0.1	0.5	0.6	0.1	4.9	-1.1	2.4	1.6
	11b	0.4	0.1	0.5	0.1	3.8	-1.0	2.5	1.5
	S13b	0.4	0.3	0.7	0.2	5.3	-1.3	3.0	1.8
16-L _b	S13c	0.4	0.4	0.8	0.2	8.0	-1.7	4.0	2.2
	S13d	0.3	0.2	0.5	0.1	3.4	-0.9	1.8	1.3
	S13e	0.1	0.5	0.6	0.1	6.1	-1.4	3.6	1.7
	S14a	0.5	0.2	0.7	0.2	6.1	-1.4	4.1	1.9
	S14b	0.3	0.4	0.7	0.1	5.2	-1.3	3.2	1.7
	S14c	0.3	0.2	0.5	0.1	5.6	-1.3	3.3	1.7
	S14d	0.3	0.2	0.5	0.1	3.7	-0.9	2.3	1.5
	11c	0.4	0.2	0.6	0.1	4.1	-1.1	2.7	1.6
18-L _a	S14e	0.4	0.3	0.7	0.1	5.0	-1.2	3.0	1.7
	S15a	0.3	0.2	0.5	0.1	4.3	-1.1	2.7	1.6
	S15b	0.2	0.5	0.7	0.1	4.7	-1.1	2.7	1.7
	S15c	0.1	0.7	0.8	1.0	6.2	-1.4	3.0	1.9
	11d	0.6	0.2	0.8	0.3	6.8	-1.5	5.5	1.9
	S15d	0.6	0.3	0.9	0.3	8.9	-1.7	5.5	2.3
	S15e	0.6	0.3	0.9	0.3	8.3	-1.7	5.9	2.4
	S16a	0.3	0.5	0.8	0.2	6.2	-1.4	3.8	1.9
	S16b	0.4	0.5	0.9	0.2	5.5	-1.4	4.4	1.8
	S16c	0.5	0.1	0.6	0.2	6.1	-1.5	3.8	1.8
18-L _b	S16d	0.3	0.6	0.9	0.2	5.1	-1.3	3.4	1.7
	S16e	0.1	0.6	0.7	0.1	3.5	-0.9	2.2	1.5
	S17a	0.0	0.8	0.8	0.1	5.5	-1.3	3.4	1.8
	11e	0.4	0.4	0.8	0.2	8.0	-1.6	4.9	2.1
19	12a	0.3	0.5	0.8	0.1	4.7	-1.1	2.9	1.6
	S17b	0.4	0.4	0.8	0.2	5.5	-1.3	4.0	1.8

(continued on next page)

Table 3 (continued)

Sample	Scan no.	CPO Strength Indices ^a				ODF Parameters ^b			Pole Figure Intensity - J Index ^c	
		P	G	B	M	J	E	<c> <0001>	<a> <11-20>	
20-L _a	S17c	0.3	0.4	0.7	0.1	6.4	-1.5	3.0	1.8	
	S17b	0.1	0.5	0.6	0.1	4.6	-1.1	2.1	1.7	
	S17d	0.2	0.3	0.5	0.1	6.2	-1.4	2.8	1.8	
	S17e	0.2	0.1	0.3	0.0	3.9	-1.0	1.9	1.4	
20-L _b	S18a	0.2	0.3	0.5	0.1	3.9	-1.0	2.5	1.5	
	S18b	0.2	0.4	0.6	0.1	3.6	-0.9	2.1	1.4	
	S18c	0.3	0.2	0.5	0.1	2.1	-0.9	2.1	1.4	
	S18d	0.2	0.3	0.5	0.1	3.2	-0.8	2.0	1.4	
	S18e	0.3	0.3	0.6	0.1	3.0	-0.7	2.1	1.4	
	S12c	0.2	0.3	0.5	0.1	3.1	-0.8	1.9	1.4	
	S19a	0.2	0.2	0.4	0.0	3.3	-0.8	1.9	1.3	
	S19b	0.2	0.3	0.6	0.1	6.4	-1.4	3.3	1.9	
22	S19c	0.1	0.4	0.5	0.0	2.9	-0.7	1.9	1.3	
	S19d	0.4	0.4	0.8	0.1	3.8	-1.0	2.5	1.5	
	S19e	0.1	0.7	0.8	0.1	3.8	-1.0	2.5	1.5	
	S19f	0.4	0.4	0.8	0.2	7.1	-1.5	3.9	2.3	

Note: a: Vollmer (1990); b: Bunge (1982), Schaeben (1988), Skemer et al. (2005); c: Michibayashi and Mainprice (2004).

MATLAB scripts of Hunter et al. (2018b) (Table 4). The OA is used to calculate the deformation temperature using the linear equations (Table 4) provided by Faleiros et al. (2016). α refers to the sense of asymmetry of the CPO fabric skeleton and thus indicates the ductile shear sense ($+\alpha$: sinistral, $-\alpha$: dextral). The S-value, on the other hand, refers to the coaxiality of deformation (0: coaxial, 1: non-coaxial; Hunter et al., 2018b). Intragranular 'neighbor-to-neighbor' low-angle ($2-10^\circ$) misorientation analysis is performed to identify active slip-systems in quartz (Neumann, 2000) and consequently the deformation temperature (Fig. 9a,b). The orientations of the misorientation axes corresponding to the intragranular neighbor-to-neighbor low-angle ($2-10^\circ$) misorientations are derived using MTEX 5.2.2 (Hiescher and Schaeben, 2008) and plotted on inverse pole figures (Figs. 10-12).

3.5.2. Crystallographic vorticity axis analysis

Ductile deformation of rocks disperses the intra-granular crystallographic axes for each grain along small circles on an equal-area lower hemisphere plot (Bestmann and Prior, 2003). The common pole to these best-fit arcs represents the vorticity axis corresponding to the grain under consideration (Fig. 1b,c of Michels et al., 2015). This technique of constraining the orientation of the bulk vorticity axis (BVA) for a specimen employing rotational statistics on the population of grain-scale vorticity axes is called the crystallographic vorticity axis (CVA) analysis (Michels et al., 2015).

If the orientations of lineations and foliations are known for the corresponding sample, CVA can aid to decipher the nature of deformations (e.g. monoclinic vs. triclinic deformation). This procedure also determines the orientation of the vorticity normal section (VNS) (BVA parallels the pole to the VNS), which is by far the most appropriate plane to identify and interpret kinematic shear sense indicators (e.g. Tikoff et al., 2013; Xypolias et al., 2018).

In this study, we used the approach that has been recently proposed by Piette-Lauzière et al. (2020). Herein, BVAs are derived separately for the recrystallized grains, the relict grains and all the grains combined. The relict and recrystallized grains are differentiated based on the 'grain orientation spread (GOS)' approach of Cross et al. (2017). Moreover, separate BVAs are deduced for the cores and rims of the relict grains in order to check whether they are homogeneously deformed or not. If not, then this method would aid in detecting signatures of an earlier deformation preserved in the cores. Finally, the BVA corresponding to the strongest CVA fabric – highest kernel density – is the most reliable one for deciphering the regional deformation kinematics (Piette-Lauzière et al., 2020).

Five BVA orientations – all grains, recrystallized grains, relict grains, relict cores and relict rims – are obtained from each thin-section. They are plotted on the specimen reference frame (SRF; Figs. 13,14). The quartz $\langle c \rangle$ -axis orientations (Figs. 10-12; Supplementary Figs. S10-S19) are then plotted on the kinematic reference frame (KRF) i.e., on the VNS (e.g. Giorgis et al., 2017).

3.5.3. Results

The values of P, G, and R (Fig. 15; Table 3) reflect the deformation intensity. P and G values increase with the intensity of deformation. Cylindricity Index ($B = 1-R$; Larson, 2018) also increases with deformation. Fig. 16a1,a2 show the variation of the mean values of B, which is >0.6 for both the transects near ZSZ implying intense deformation. The Symmetry value (S) obtained from the quartz CPO plots are 'semi-quantitative' measure of the non-coaxiality of the deformation. It ranges from 0 (non-coaxial) to 1 (purely coaxial) (Hunter et al., 2018b). For all the samples, except the one from location 20, the mean values of S are <0.5 (Fig. 16b1,b2; Table 4) indicating dominantly non-coaxial deformation.

Deformation temperatures calculated from the linear equations of Faleiros et al. (2016) provide wide ranges for both the transects (A: $\sim 450-800^\circ\text{C}$; B: $\sim 250-750^\circ\text{C}$) (Table 4). Temperatures deduced from the graph of Morgan and Law, 2004 (Fig. 17) illustrate that majority of

Table 4
 Quartz CPO derived S-values, obliquity angle (α), opening angle (OA) and deformation temperatures. Slip-system are identified from low angle (2-10°) intragranular ‘neighbor to neighbor’ misorientation analysis. For the locations see Fig. 1. Figure numbers starting with S refer to Supplementary Figures (S10-S19).

Sample	Fig.	Shear towards	Quartz CPO Pole Figure (Kinematic Reference Frame)					Slip-system		
			Symmetry Value (S-value)	Obliquity Angle (α , °)	Opening Angle (OA, °)	Deformation Temperature		All Grains	Recrystallized Grains	Relict Grains
						Falerios et al. [§] (2016)	Morgan & Law [#] (2004)			
6-L _a	S10a	NNW	0.7	-55.0	99.0	713.4	-	{r}(a)	{r}a, {m}c	{r}(a)
	S10b	SSE	0.4	-23.0	71.5	541.4	569.7	[c](a)	[c](a)	{r}(a)
	S10c	NNW	0.6	26.0	86.5	644.9	689.2	{m}(a), π' a	{m}(a), π' a	{z}(a)
	10a	NNW	0.5	-79.0	118.0	800.8	-	[c](a), {r}(a)	[c](a), {r}(a)	π' (a)
6-L _b	10b	SE	0.1	-33.0	114.0	782.4	-	{m}(c)	π' (a)	{m}(c)
	S10d	NW	0.0	-59.0	100.0	718.0	-	[c](a)	{m}(c)	[c](a)
	S10e	SE	0.2	-31.0	71.0	537.9	565.7	π' (a)	{m}(c)	π' (a)
9	S11a	W	0.5	-42.0	86.5	644.9	689.2	{r}(a)	[c](a)	{r}(a)
	S11b	W	0.4	-41.0	86.5	644.9	689.2	{r}(a)	{r}(a)	{r}a, [c]a
	10c	W	0.0	-36.0	97.0	704.2	-	[c](a)	[c](a)	{r}(a)
11-L _a	S11c	SE	0.3	-23.0	83.5	624.2	665.3	{m}(c), π' (a)	{m}(c)	π' (a), {m}(a), {z}(a)
	S11d	SE	0.4	-17.0	75.5	569.0	601.6	{r}(a), π' (a)	{r}(a), π' (a)	{z}(a)
	10d	SE	0.3	49.0	112.0	773.2	-	π (a), π' (a)	π (a), π' (a)	π (a), π' (a)
11-L _b	S11e	SW	0.4	-49.0	66.0	503.4	525.9	{m}(c+a)	{m}(c+a)	{m}(c+a)
	10e	SW	0.0	11.0	57.5	444.8	458.2	{m}(a)	{m}(a)	{m}(c), {r}(a)
	S12a	SW	0.4	27.0	60.0	462.0	478.1	{z}(a), π (a)	π (a)	π (a)
15	S12b	ENE	0.1	-15.0	83.5	624.2	665.3	π' (a)	{m}(a), {m}(c)	π' (a), {z}(a)
	11a	WSW	0.1	6.0	84.0	627.6	669.3	{m}(c)	{m}(c)	[c](a)
16-L _a	S12c	NW	0.3	2.0	57.0	441.3	454.2	[c](a)	[c](a)	-
	S12d	NW	0.1	30.0	58.0	448.2	462.2	{m}(c), {z}(a)	{z}(a)	{m}(c), {z}(a)
	S12e	NW	0.2	31.0	57.0	441.3	454.2	{m}(a), {m}(c)	{m}(a), {m}(c)	{m}(a), {m}(c)
	S13a	SE	0.3	-32.0	54.0	420.6	430.3	{m}(a)	{m}(a)	{m}(a)
	11b	NW	0.8	19.0	60.5	465.5	482.1	π' (a)	π' (a)	{m}(a), [c](a)
	S13b	SE	0.5	-27.0	55.0	427.5	438.2	{m}(c)	{m}(c)	{m}(c)
16-L _b	S13c	NW	0.3	-60.0	60.0	462.0	478.1	{r}(a)	{r}(a)	{m}(c)
	S13d	NW	0.8	42.0	66.0	503.4	525.9	{m}(a), π' (a)	{m}(a), π' (a)	{m}(a), π' a
	S13e	SE	0.3	72.0	98.0	708.8	-	{r}(a)	{r}(a)	{z}(a)
	S14a	SE	0.1	-42.0	73.0	551.7	581.7	{m}(c), [c](a)	{m}(c), [c](a)	{m}(c), [c](a)
	S14b	SE	0.3	-43.0	102.5	729.5	-	{m}(c+a)	{m}(c+a)	{r}(a), {m}(c+a)
	S14c	NW	0.3	19.0	49.5	389.6	394.4	[c](a)	[c](a), {m}(a)	[c](a), π' (a)
	S14d	NW	0.3	23.0	75.5	569.0	601.6	{z}(a)	{z}(a)	{m}(c)
	11c	SE	0.8	-42.0	53.0	413.7	422.3	{z}(a)	{z}(a)	{m}(c+a), {z}a
18-L _a	S14e	SSE	0.1	32.0	83.0	620.7	661.4	{m}(a)	[c](a)	{m}(a)
	S15a	NNW	0.3	48.0	73.5	555.2	585.7	{m}(a)	[c](a)	{m}(a), {m}(c)
	S15b	SSE	0.4	-72.0	83.0	620.7	661.4	{z}(a)	[c](a)	{z}(a)
	S15c	SSE	0.6	-88.0	93.0	685.8	-	{m}(a)	{m}(a)	{m}(a)
	11d	NNW	0.2	-36.0	72.0	544.8	573.7	{z}a	{z}(a)	[c]a, {m}(c+a)
	S15d	NNW	0.0	-36.0	68.5	520.7	545.8	[c](a)	[c](a)	[c](a)
	S15e	NNW	0.3	-22.0	72.0	544.8	573.7	π (a)	π (a)	{m}a, [c]a
	S16a	SSE	0.2	-65.0	107.5	752.5	-	{m}(a)	{m}(a), [c](a)	{m}(a), {z}(a)
	S16b	SSE	0.5	-49.0	65.5	500.0	521.9	{z}(a)	{z}(a)	[c](a), {r}(a)
	S16c	SSE	0.1	42.0	98.0	708.8	-	{m}(c+a)	{m}(c+a)	{m}(a)
18-L _b	S16d	W	0.7	5.0	107.5	752.5	-	{m}(c)	π (a)	{m}(c)
	S16e	W	0.4	-57.0	79.5	596.6	633.5	[c](a)	[c](a)	{m}a, [c](a)
	S17a	E	0.3	78.0	95.0	695.0	-	{r}a, [c]a	{r}a, [c]a	[c](a)
	11e	W	0.1	-60.0	97.0	704.2	-	{r}(a)	{r}(a)	{r}(a)

(continued on next page)

Table 4 (continued)

Sample	Fig.	Shear towards	Quartz CPO Pole Figure (Kinematic Reference Frame)				Deformation Temperature		Slip-system	
			Symmetry Value (S-value)	Obliquity Angle (α_r , °)	Opening Angle (OA, °)	Faleiros et al. (2016)		All Grains	Recrystallized Grains	Relict Grains
						Morgan & Law* (2004)	Morgan & Law* (2004)			
19	12a	E	0.0	-18.0	71.5	541.4	569.7	{r}(a)	{r}(a)	{r}(a)
	S17b	E	0.1	-32.0	77.5	582.8	617.5	{r}(a)	{r}(a)	{z}(a)
	S17c	E	0.1	-34.0	81.0	606.9	645.4	{c}(a), {z}(a)	-	{c}(a), {z}(a)
20-1 _a	12b	W	0.5	23.0	51.5	403.4	410.4	{r}(a), {m}(c)	{m}(c)	{r}(a)
	S17d	W	0.8	26.0	58.0	448.2	462.2	{c}(a), {r}(a)	{c}(a), {m}(c)+a	{z}(a), {r}(a)
	S17e	E	0.8	-18.0	53.0	413.7	422.3	{c}(a)	{c}(a)	{c}(a), {m}(c)+a
	S18a	W	0.2	38.0	46.0	365.4	366.5	{c}(a), {z}(a)	{c}(a), {r}(a)	{r}(a)
20-1 _b	S18b	W	0.7	5.0	61.0	468.9	486.1	{m}(a)	{m}(a)	{c}(a)
	S18c	W	0.7	1.0	31.5	265.4	251.0	{r}(a)	{r}(a)	{r}(a)
	S18d	W	0.7	14.0	47.5	375.8	378.5	{m}(a)	π (a), {m}(c)+a	{r}(a)
	S18e	W	0.1	-50.0	102.5	729.5	-	{m}(c), {m}(a)	{m}(c), {m}(a)	{m}(c), {r}(a)
	12c	-	0.4	0.0	88.0	662.8	-	{r}(a)	{r}(a)	{r}(a)
	S19a	W	0.6	4.0	51.5	403.4	410.4	{m}(a)	{m}(a)	{m}(a)
	21	12d	NE	0.1	-35.0	57.0	441.3	454.2	{m}(a)	{r}(a)
S19b	SW	0.6	37.0	65.0	496.5	517.9	{r}(a)	{r}(a), {m}(c)	{r}(a), {m}(c)	
22	12e	NE	0.9	-20.0	41.0	330.9	326.7	{m}(a)	{m}(a)	{m}(a)
	S19c	NE	0.0	-15.0	94.0	690.4	-	{z}(a)	{z}(a)	{z}(a)
	S19d	NE	0.6	-32.0	74.5	562.1	593.6	{m}(a)	{m}(a)	{m}(a)

Note: §: The following equations of Faleiros et al. (2016) are used to compute deformation temperatures

T (°C) = 6.9 × OA (°) + 48 (OA ≤ 87°); T (°C) = 4.6 × OA (°) + 258 (OA ≥ 87°)

#: Deformation temperatures are calculated only for pole figures with OA ≤ 87° from the OA v/s temperature graph of Morgan and Law (2004).

the data from the two transects lie >400 °C. Low-angle (2–10°) intra-granular neighbor-to-neighbor misorientation analysis, on the other hand, show that high temperature prism-(a) (500–700 °C; Fig. 9a) and prism-(c) (> 650 °C; Fig. 9a) slip-systems are more common for samples from Transect-B (Table 4). Microtextural evidences of incipient partial melting at >650 °C are also prevalent in Transect-B samples (Fig. 18).

CVA fabric derived from the relict grains are considerably stronger than that of recrystallized grains and all grains, for all the locations (Figs. 13,14). Relict cores and rims exhibit CVA fabric comparable to that of the relict grains, but are weaker. For a few samples (locations 9, 11, and 16), the CVA fabric obtained from the rims are slightly higher than that of the entire relict grains, but the BVA orientations are near similar in all such cases (Table 5). BVAs derived from the relict grains are more reliable since the corresponding CVA fabrics are the strongest (Piette-Lauzière et al., 2020), and hence we chose them to decipher the deformation kinematics. Angular relationships between the BVA – derived from the relict grains – and the rock fabrics exhibit evidences of either simple-shear dominated transpression at some locations e.g. locations 6 (Fig. 13a,b) 9 (Fig. 13c), 15 (Fig. 13f), 19 (Fig. 14c) or triclinic (transpressive) e.g. locations 11 (Fig. 13e), 16 (Fig. 13g), 18 (Fig. 14b), 20 (Fig. 14e) and 21 (Fig. 14f) (Table 5).

Moreover, the BVA orientations are chosen to plot the quartz CPO pole figures in the KRF (Figs. 10–12, Supplementary Figs. S10–S19). Since stretching lineations may not parallel the VNS, the ductile shear senses deciphered from the pole figures plotted in the KRF (Figs. 10–12) have only been considered for kinematic analyses in this study. Opposite shear senses are noted on the VNS for all the samples except for locations 9, 19 and 22. (Figs. 1, 19). There is at least one pair of OSS from all other locations (Table 5).

4. Discussions

The terrane is polydeformed (at least 3 phases; Supplementary Table S2). However, both Guillot et al. (1997) and de Sigoyer et al. (2004) proposed that the penultimate phase (D2; syn-extrusional) was stronger than the rest and hence is predominantly preserved in the gneiss. Likewise, Epard and Steck (2008) reported that the first deformation phase D1 (post-UHP, also syn-extrusional), produced the dominant schistosity in the gneiss. Hence, our interpretations on the flow kinematics reflect that of the strongest, syn-extrusional deformation phase.

4.1. Deformation mechanism, temperature & intensity

The abundance of mylonitic, fine-grained quartzo-feldspathic (microlithon) domains is high in the samples near the N margin of the TMC. This could either be an artefact of increased micro-scale strain partitioning (Larson et al., 2014) or elevated strain intensity (White & Lennox, 2010). Since the northern margin is also a shear zone, we support the latter. Grain parameters (Section 3.4) measured from the recrystallized quartz grains and the P, G, and R values of the EBSD-derived pole figures also demonstrate the same. However, unlike the predictions of the channel flow model, none of these reveal any distinct pattern of variation of the deformation intensity across the TMC.

Schlup et al. (2003) proposed that the central part (Transect-A of this study) of the TMC crossed 300 °C isotherm at least ~10 Ma earlier than the western part (Transect-B of this study). This implies that the gneissic samples of Transect-B must preserve more evidences of higher deformation temperature. Our observations concur with this. We note the prevalence of prism-(a) (500–700 °C; Fig. 9a) and prism-(c) (> 650 °C; Fig. 9a) slip-systems in the samples of Transect-B (Table 4) along with high grain lobateness (PARIS factor; Table 2). The published extrusion models for the TMC (Section 1), however, do not explain this spatial variation in deformation temperatures. Hence, those must be updated accordingly.

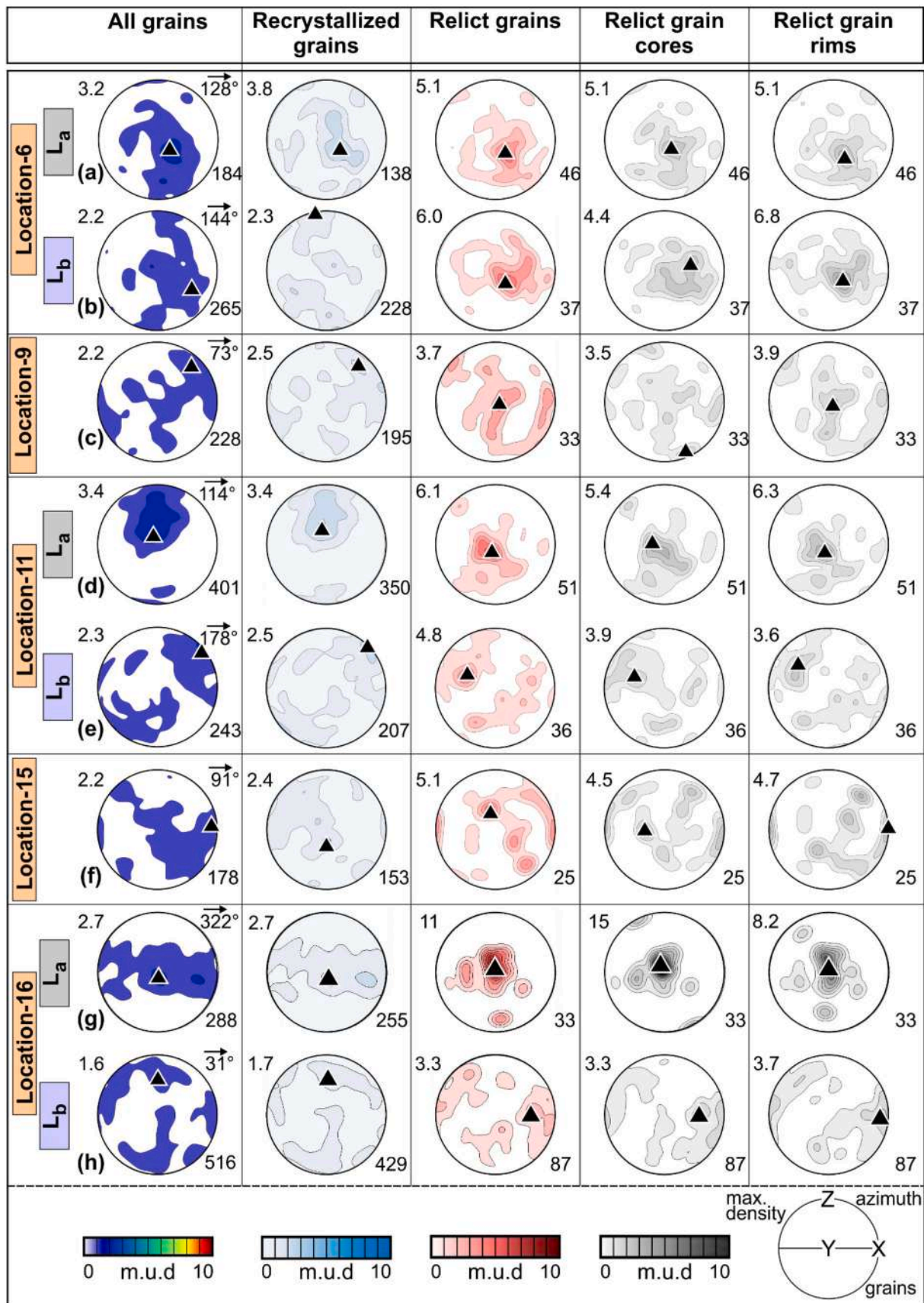


Fig. 13. Selected results of the crystallographic vorticity axis (CVA) analysis for locations 6, 9, 11, 15, and 16. The equal area, lower hemisphere pole figures are plotted on sample reference frames (SRF; also shown in the bottom right corner). The black triangle represents the bulk vorticity axis (BVA).

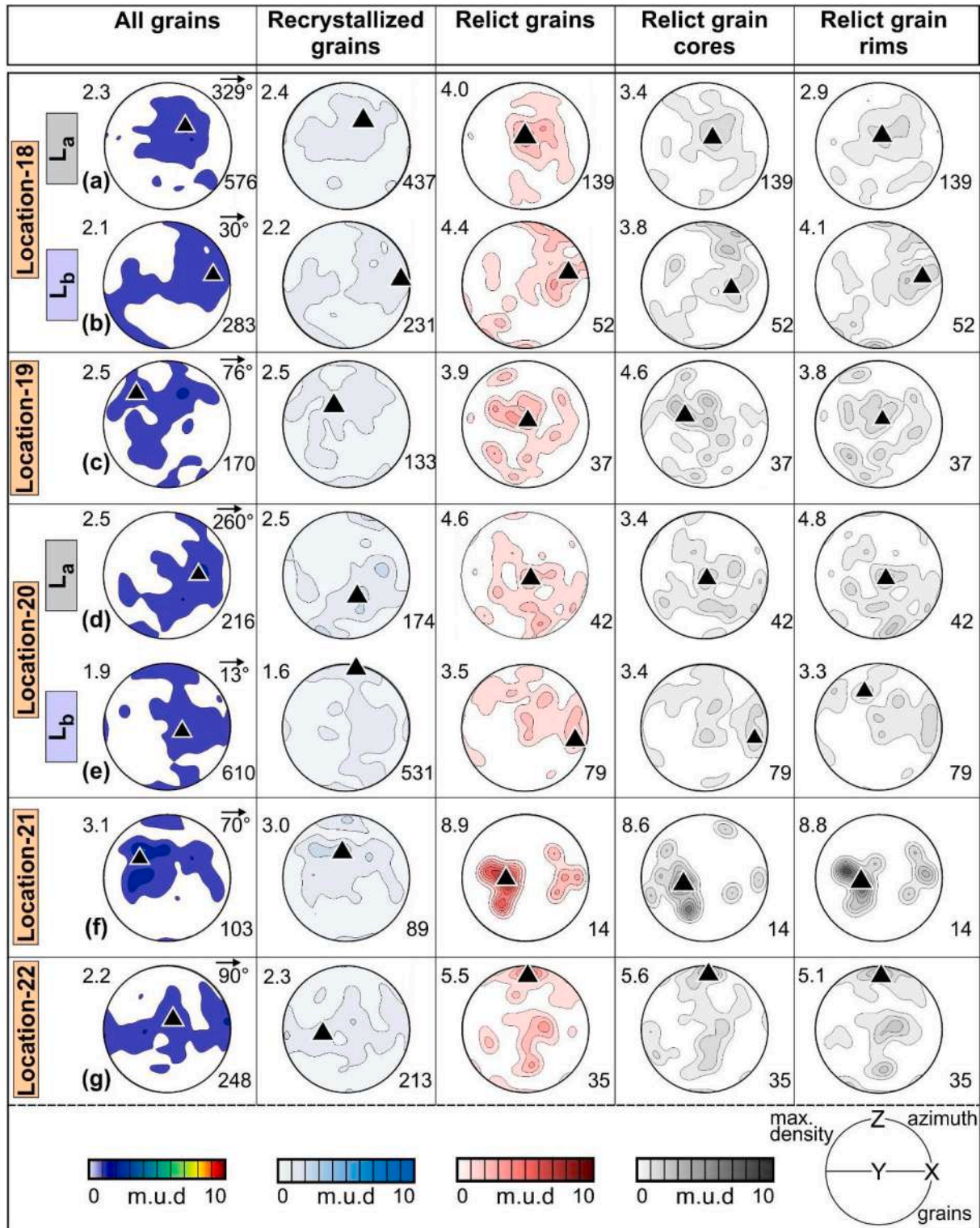


Fig. 14. Selected results of the crystallographic vorticity axis (CVA) analysis for locations 18, 19, 20, 21, and 22. The equal area, lower hemisphere pole figures are plotted on sample reference frames (SRF; also shown in the bottom right corner). The black triangle represents the bulk vorticity axis (BVA).

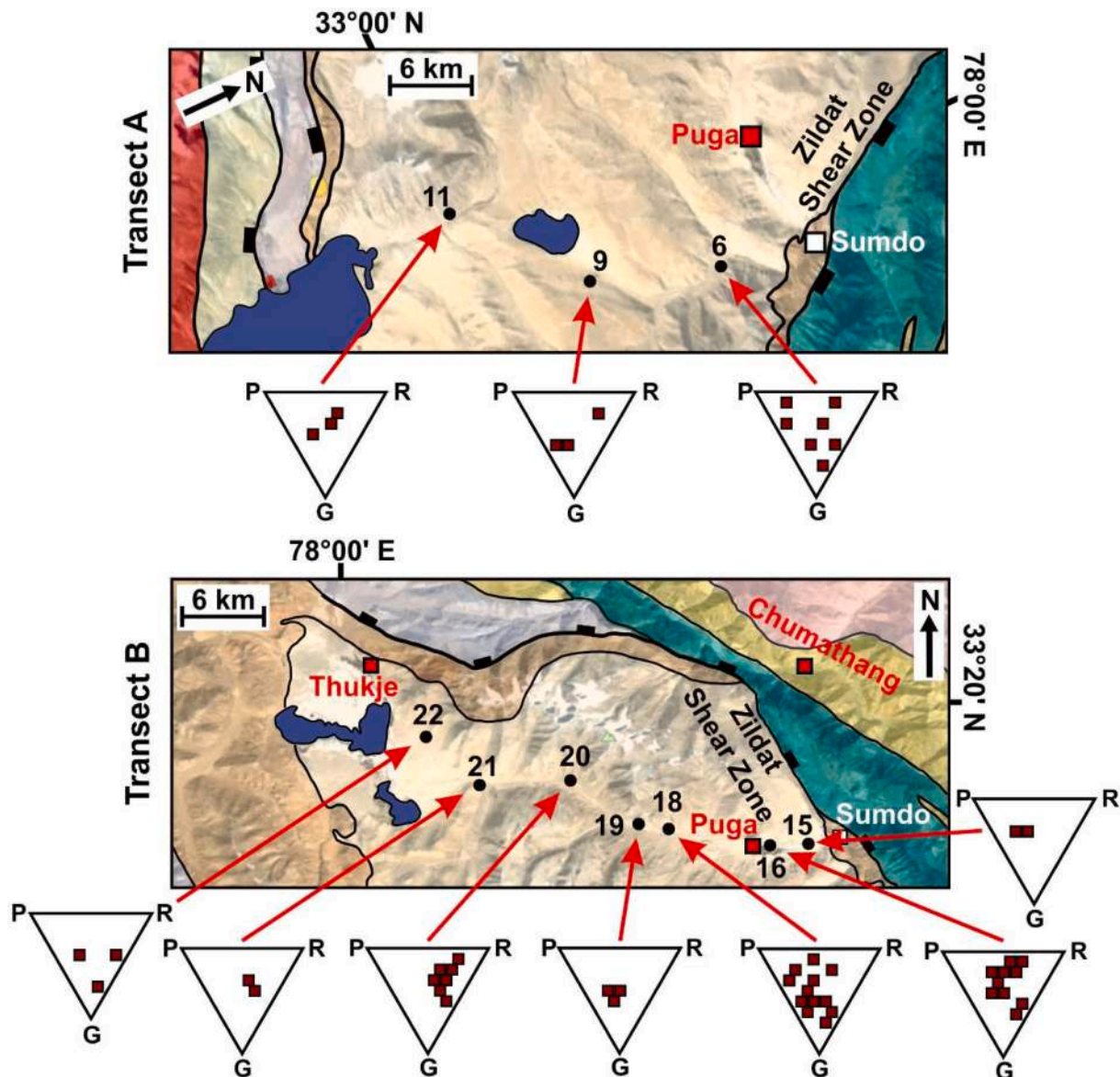


Fig. 15. PGR ternary plots for the samples derived from the EBSD based quartz CPO analysis (Table 3).

4.2. Fluid activity & possibility of partial melting

Deformation-induced fluid flow may result in muscovitization of feldspars in the vicinity of shear zones (Hemley and Jones, 1964; Wiberley, 1999), such that the feldspar:muscovite ratio rises with increasing shear strain. XRD analysis of samples (Section 3.2) close to the ZSZ illustrate the same (Fig. 4, Supplementary Fig. S5), thereby implying the elevated shear intensity near the ZSZ.

Partial melting of the gneiss, although less discussed (Palin et al., 2017), could not be refuted (Fig. 18). The P-T path reported by St-Onge et al. (2013) – derived from a sample near to location 6 in Fig. 1 – intersects the dehydration melting curve of muscovite (curve b in Fig. 2a). The authors dated this event to ~45 Ma (line iii in Fig. 2c, Supplementary Table S4). Furthermore, cusped/arcuate boundaries between K-feldspar and quartz grains, possible indicators of partial melting (Chen et al., 2013), are also identified (Fig. 18). Low-angle (2–10°) misorientation analysis (Section 3.5.1) predicts temperature > 650 °C (prism-c) slip, Figs. 10–12, Table 4) from locations 6, 15, 16, 11 and 20. These observations, when compared with the P-T path of St-Onge et al. (2013)

in Fig. 2, suggest that the gneissic rocks of the TMC may have suffered ‘fluid absent melting’ (Weinberg and Hasalová, 2015) at ~45 Ma. This could have lowered the viscosity of the TMC thereby facilitating the extrusion (Labrousse et al., 2002) post thermal peak conditions. However, quantification of the partial melt volume and the extent of viscosity reduction would require further studies.

4.3. Opposite shear senses

Kinematic indicators of ductile-shear are identified from the thin-sections (Fig. 7), and convincing evidences of OSS are noted. However, we do not encounter any cross-cutting relation between the shear planes, which may suggest that their development are coeval. OSS from quartz pole figures (in the KRF) are observed from the central portion and the margins of the TMC (Section 3.5.3) except the locations 9, 19 and 22 (Fig. 1; Table 5). In some samples the two shear senses seem to be coeval based on the temperature range derived for both (from the low-angle misorientation analysis; Table 4) viz. *top-down-to-SE* and *top-up-to-NW* at location 6 (> 500 °C, BVA-plunge direction/ plunge amount: 30°/

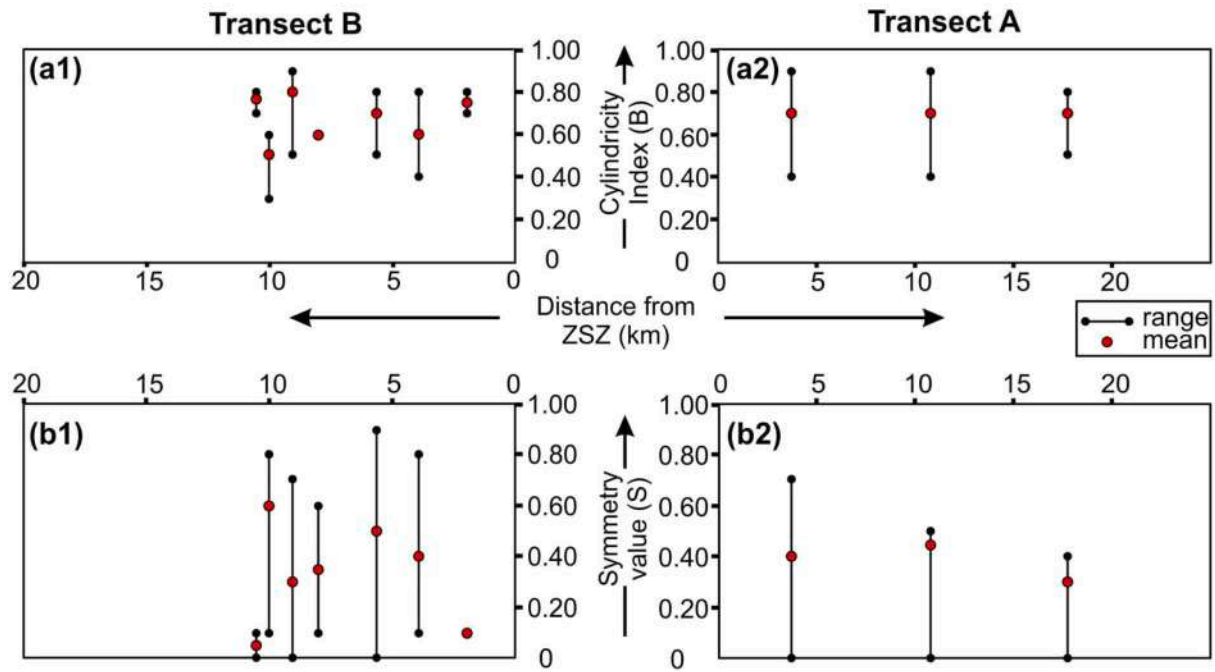


Fig. 16. Variations in the (a1,a2) Cylindricity Index (B) and the (b1,b2) Symmetry values (S) with distance from the ZSZ along the two transects.

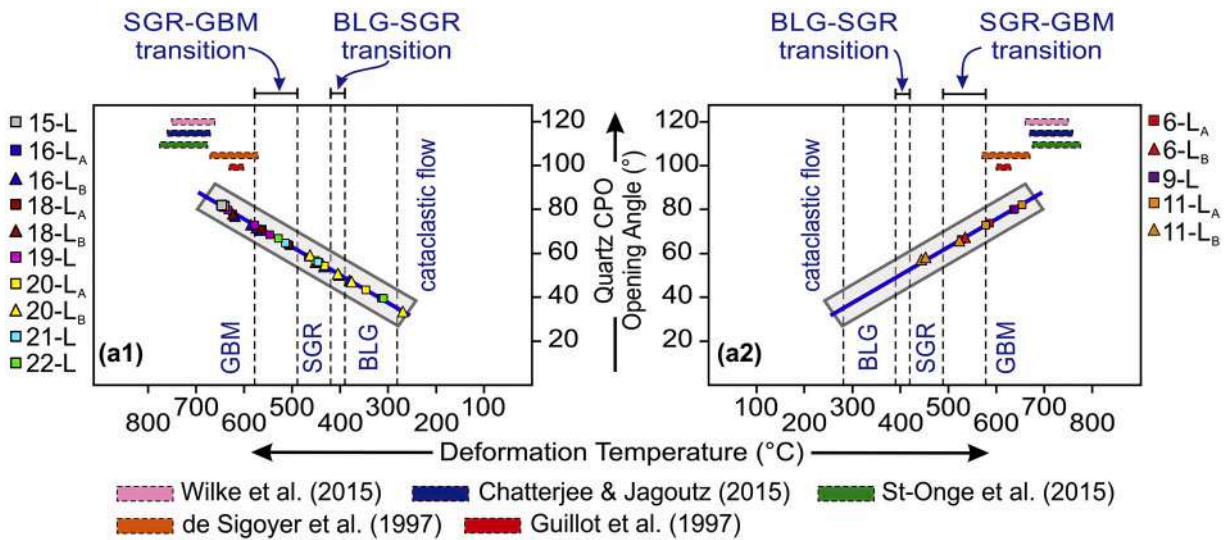


Fig. 17. Deformation temperatures for the samples derived from the opening angles (OA) of the quartz CPO pole figures (Fig. 10-12) using the geothermometer of Kruhl (1998) and Morgan and Law (2004). The quartz recrystallization regimes are also demarcated (Stipp et al., 2002a, 2002b). The pink, blue, green, orange, and red colored rectangles inside the graphs represent the ranges of the peak temperature attained by the TMC as estimated by Wilke et al. (2015), Chatterjee and Jagoutz (2015), St-Onge et al. (2013), de Sigoyer et al. (1997), and Guillot et al. (1997), respectively (see Supplementary Table S3 for details).

56°), *top-down-to-NW* and *top-up-to-SE* at location 16 (> 500 °C, BVA: 57°/7°), and *top-down-to-W* and *top-up-to-E* at location 18 (300–400 °C, BVA: 355°/14°).

Coaxial deformation also produces coeval OSS (Little et al., 2013, review in Dutta and Mukherjee, 2019). However, this study does not show bulk pure shear-dominated deformation (Figs. 13,14; Table 5). On the other hand, fluid or melt induced viscosity inhomogeneity may lead to coeval development of OSS at grain-scale under general shear (Hipperth and Tohver, 1999; review in Dutta and Mukherjee, 2019). We suspect that the incipient partial melting of the gneiss (Section 4.2) could

have varied the viscosity locally, producing coeval OSS at grain-scale.

4.4. Nature of flow: triclinic?

EBSD-based CVA analysis produces results of the last deformation of ‘significant strain’, and is unlikely to be affected by later deformations of lower strain magnitude. The varied dispersion of the BVAs from one location to another across the TMC (Fig. 19; Table 5) could be the result of deformation partitioning or maybe a temporal variation in BVA orientation during progressive deformation. In such a scenario, a modal

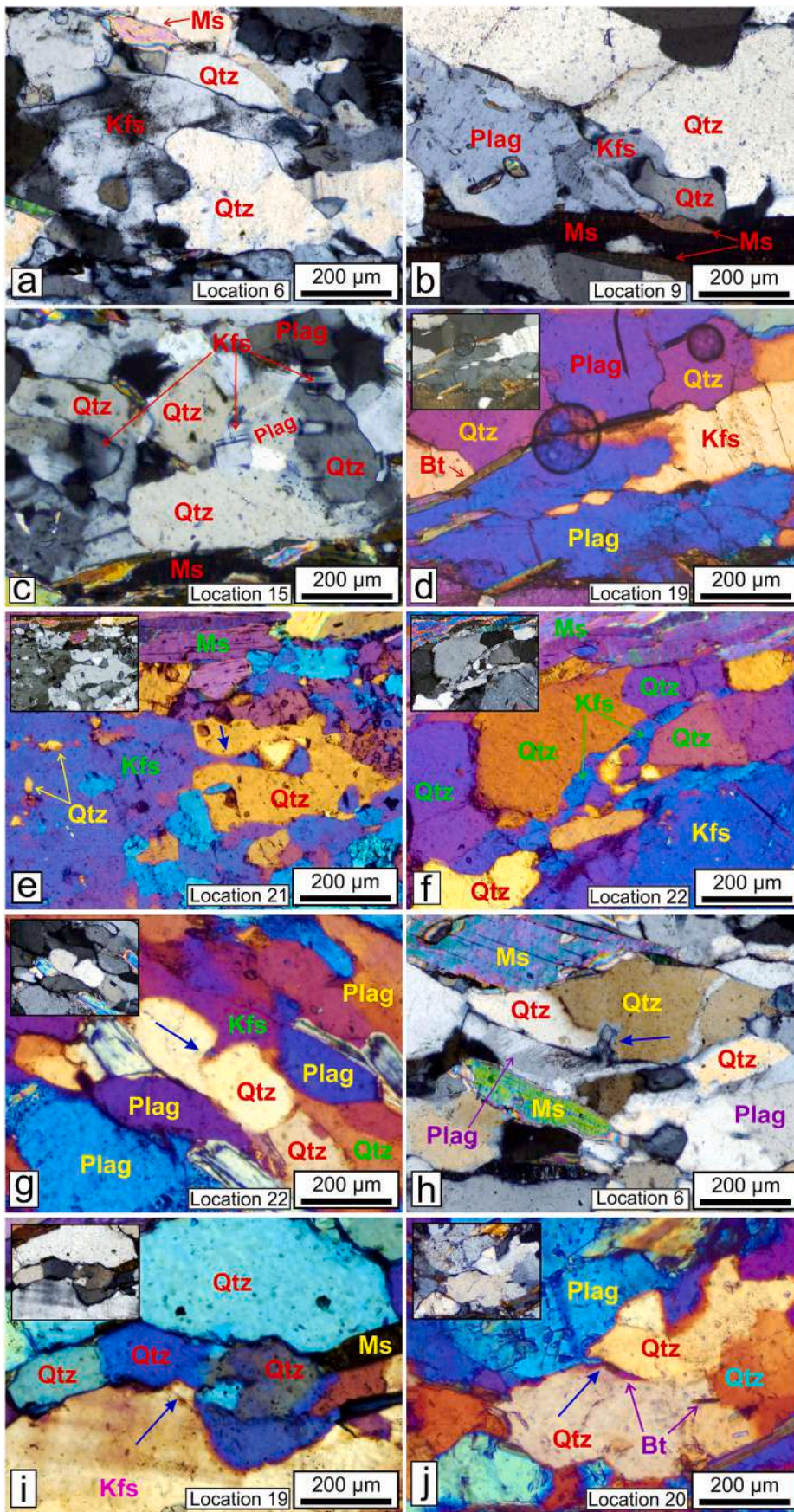


Fig. 18. Microstructural evidences of possible partial melting in the gneissic host (also see Supplementary Fig. S20 for comparison). (a) Cusped Kfs-Qtz grain boundary. The Kfs occurs as a melt pocket between quartz grains (XPL), (b) Curved/arcuate boundary between Kfs and quartz grains (XPL), (c) Pockets of Kfs surrounded by quartz & plagioclase grains with sub-rounded grain boundaries. Also note the highly cusped Kfs-qtz grain boundary to the left (XPL), (d) Possible squeezing of Kfs (melt pseudomorph) along plagioclase subgrain boundary (image with gypsum plate). Inset shows the XPL image, (e,g,i) Kfs (melt pseudomorph) along the quartz subgrain boundary (blue arrows). Note the rounded boundary of quartz and the quartz inclusions in the Kfs grain (to the left) in (e) (image with gypsum plate). Inset shows the XPL image, (f) Kfs (melt pseudomorph) in between quartz grains with sub-rounded boundaries (image with gypsum plate). Inset shows the XPL image, (h,j) Former melt (?) along the quartz subgrain boundaries (blue arrows). Inset shows the XPL image. Mineral abbreviations: Bt – Biotite, Kfs – K-feldspar, Ms. – Muscovite, Plag – Plagioclase, and Qtz – Quartz. (For interpretation of the references to colour in this figure legend, the reader is referred to the web version of this article.)

Table 5
Results of crystallographic vorticity axis (CVA) analysis (BVA: Bulk Vorticity Axis). See Fig. 1 for locations. All trend and plunge values are in degrees.

Sample.	Lineation		CVA Analysis				BVA orientations					
			All grains		Recrystallized grains		Relict grains		Relict core		Relict rim	
	trend	plunge	trend	plunge	trend	plunge	trend	plunge	trend	plunge	trend	plunge
6-I _a	128	21	77	60	79	58	70	63	60	57	79	69
6-I _b	144	6	108	62	250	38	30	56	67	39	40	57
9	73	14	92	61	94	62	171	7	9	67	168	5
11-I _a	114	9	26	14	26	22	27	7	220	3	27	8
11-I _b	178	8	347	30	349	35	309	6	309	3	314	17
15	91	4	93	6	1	3	347	47	330	18	91	3
16-I _a	322	8	46	6	44	5	57	7	60	10	58	6
16-I _b	31	9	126	48	123	49	67	7	70	6	41	6
18-I _a	329	30	252	32	260	34	251	5	244	12	249	10
18-I _b	30	16	359	13	13	17	355	14	332	33	356	17
19	76	8	290	36	326	29	350	3	355	33	352	2
20-I _a	260	10	303	33	332	5	352	35	352	31	352	37
20-I _b	13	23	293	32	148	48	353	39	354	40	97	31
21	69	7	297	31	329	39	315	4	312	7	316	8
22	90	8	10	18	177	22	298	85	305	86	296	85

BVA – that indicates the preferred orientation based on the kernel density estimate from all the BVAs – could be a better representation of the overall deformation kinematics. Similarly, modal lineation and foliation are also derived using the Fabrica toolbox (<https://github.com/zmichels/Fabrica>). The obliquity between the modal BVA (trend / plunge: 351°/40°) to the modal lineation (trend / plunge: 76°/8°), and the modal foliation (dip / dip direction: 10°/41°) also suggest an overall triclinic symmetry of deformation (Fig. 20a) in the TMC.

As discussed in Sec. 3.5.3, several locations e.g. 11 (Fig. 13e), 16 (Fig. 13g), 18 (Fig. 14b), 20 (Fig. 14e) and 21 (Fig. 14f) (Table 5) show evidences of triclinic deformation, whereas simple-shear dominated transpression is evident at a few others e.g. locations 6 (Fig. 13a,b) 9 (Fig. 13c), 15 (Fig. 13f), 19 (Fig. 14c). It is possible for localised preservation of (pseudo-) monoclinic symmetries during an overall triclinic deformation under high shear strains when the vorticity axis parallels the lineation (Díaz-Azpiroz et al., 2019). The proximity of the locations 6, 9 and 15 to the northern boundary of the subduction channel might have resulted in elevated shear strains and the (pseudo-) monoclinic symmetry. It must be noted that the dispersion of stretching lineations on sub-horizontal folia – as encountered in the TMC (Fig. 4) – also imply complex triclinic shear (Xypolias et al., 2018).

4.5. Plausible extrusion mechanism: channel-flow or diapiric or any other?

The extrusion mechanism of the TMC is widely debated. Three noteworthy models have been proposed so far: (i) ductile wedge extrusion (Epard and Steck, 2008), (ii) buoyancy-driven channel flow (Beaumont et al., 2009), and (iii) diapirism (Chatterjee and Jagoutz, 2015). The second one is largely accepted since the other two fail to explain the upper crustal structures viz., antiformal dome with the UHP nappe at the core and overlain by low-grade rocks, *syn*-extrusion normal faults and hinterland-dipping thrust faults (Beaumont et al., 2009). Below, we discuss the extrusion kinematics of the TMC compiling the interpretations presented so far, followed by the model itself.

BVA orientations derived from EBSD-based CVA analysis (Sec. 3.5.2), when compared to the foliations and lineations, exhibit evidences of triclinic deformation, and so does the obliquity between the modal BVA (trend / plunge: 351°/40°), modal foliation (dip / dip direction: 10°/41°) and the modal lineation (trend / plunge: 76°/8°) (Sec. 4.4). We also identify that the best-fit girdle for all the lineations in the gneiss (dip / dip direction: 5°/76°; Fig. 15a) is at a low angle to the modal foliation (dip / dip direction: 10°/41°; Fig. 15a). Such a great circle dispersion of stretching lineations, although a controversial topic, has been characteristically reported from transpressional shear zones (Xypolias et al., 2018). Jones et al. (2004) further asserted that triclinic deformation with low 'transpressional shortening' will always result in intermediate pitch ($\neq 0, 90^\circ$; Fig. 6 of Jones et al., 2004) of the lineations on the foliation planes – similar to that observed in the TMC (Fig. 4).

We propose that the TMC extruded obliquely along an upward-diverging channel (Fig. 20b). This extrusion was triggered (at ~54 Ma) by the return flow at the channel bottom (Cloos, 1982) and buoyancy of the TMC. But, significant upward push was generated due to the continued oblique collision between the Indian and the Eurasian plates. This possibly resulted in a non-planar, triclinic transpression, such that the spatial variation of the extrusion direction could also have contributed to the diverse shear senses observed at both meso- and micro-scales. However, constraining the angular variation of the extrusion direction is beyond the scope of this study and has not been derived. This extrusion, as per Guillot et al. (2000, 2001), was facilitated by the 'lubricating effect' of serpentinites present to the north of the TMC. Additionally, quartz CPO and CVA studies do not demonstrate bulk coaxial deformation during extrusion. Hence, diapiric ascent of the TMC through the overlying mantle wedge – as suggested by Chatterjee and Jagoutz (2015) – seems unlikely.

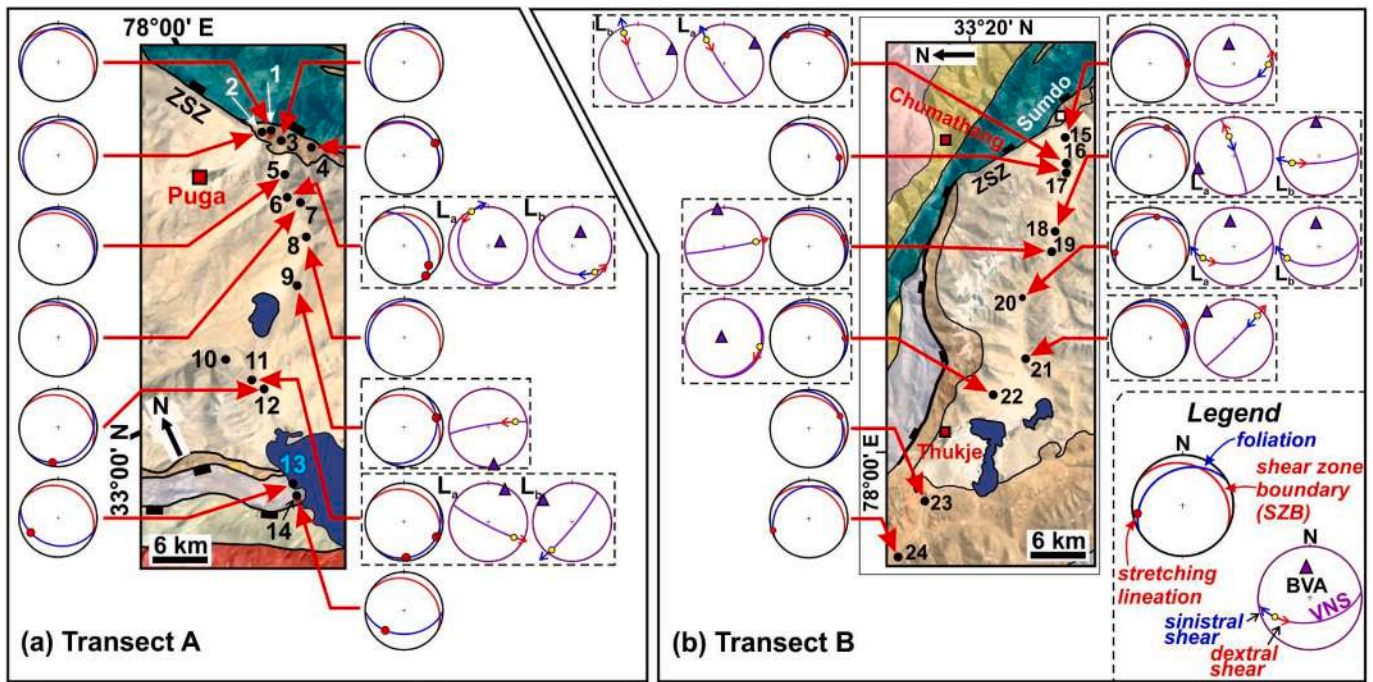


Fig. 19. Stereoplots showing orientations of various meso- (black bordered stereonet) and micro- (purple bordered stereonet) scale fabrics from all the locations along with the shear senses as determined from quartz CPO pole figures plotted in the KRF (Fig. 10-12, Table 4; Supplementary Figs. S10-S19). Also see Table 5. (For interpretation of the references to colour in this figure legend, the reader is referred to the web version of this article.)

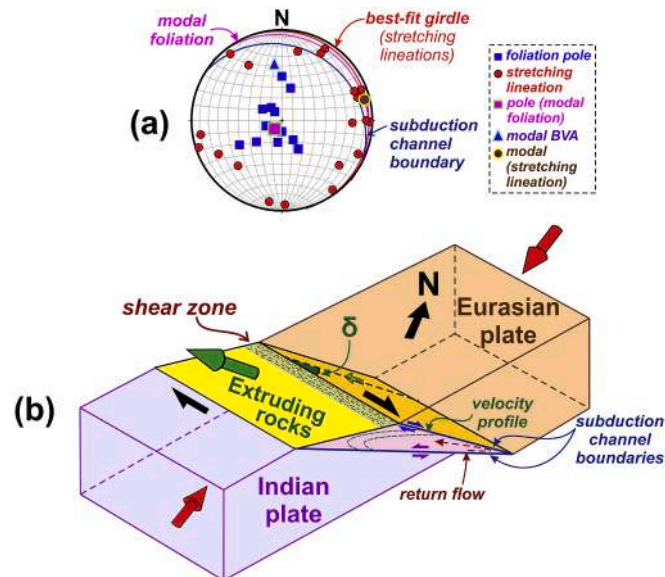


Fig. 20. (a) Stereoplots with all the foliation poles, lineations and their corresponding modal vectors (see Sec. 4.4). The best-fit girdle for the lineations is also plotted. (b) Schematic diagram of the tectonic model proposed in this study for the exhumation of the TMC. δ is the pitch of the extrusion direction on the subduction channel boundary (SCB). The velocity profile in (b) is as per fig. 8a of Grujic et al. (1996). The red arrows indicate the regional compression direction in the NW Himalaya that has remained nearly constant since the Indian and the Eurasian plates collided at ~ 54 Ma (Copley et al., 2010; van Hinsbergen et al., 2011). The SCBs dip gently and can be safely assumed to parallel each other over a vertical depth of ≥ 100 km (maximum depth calculated from the TMC eclogites, see Fig. 2). Hence, they are represented by a single girdle in (a). (For interpretation of the references to colour in this figure legend, the reader is referred to the web version of this article.)

5. Conclusions

We study the syn-extrusion deformation and flow kinematics of the UHP eclogite-bearing gneisses of the TMC. Field observations combined with petrographic studies indicate high ductile shear intensity near the northern margin (Zildat Shear Zone) – which also represents the upper margin of the subduction channel – of the TMC. XRD analysis of the

gneisses collected from the vicinity of the shear zone indicate elevated fluid activity. We suggest this to be a consequence of intense shear deformation. Fine grain-size of recrystallized quartz grains and the strong intensity of the EBSD-derived pole figures also reflect the same. However, unlike the channel flow model, they do not reveal a decline in deformation intensity away from the margins and towards the centre of the TMC.

Low-angle (2–10°) intragranular 'neighbor-to-neighbor' misorientation axes analysis, along with the microtextural evidences of incipient partial melting, imply that the gneisses must have attained >600 °C, probably ~45 Ma. CVA analysis recognize evidences of triclinic deformation during the extrusion. Obliquity of the modal BVA to the modal lineation and foliation also suggest the same.

We propose that the TMC extruded obliquely along an upward-diverging channel. The extrusion was triggered by the return flow at the channel bottom and buoyancy of the TMC, and facilitated by the upward push generated due to the Indo-Eurasia collision. The extrusion mechanism could thus resemble a combination of both channel flow and ductile wedge extrusion. Continued convergence possibly promoted a non-planar and triclinic (transpressive) deformation in a way that the extrusion direction varied spatially and the diverse shear senses observed at both meso- and micro-scales.

Declaration of Competing Interest

The authors declare that they have no conflict of interests that could have appeared to influence the work reported in this paper.

Acknowledgements

This article is a part of DD's Ph.D. thesis (Dutta, 2020) supported by the University Grants Commission's (New Delhi, India) Junior Research Fellowship grant number: F. 2-2/1998 (SA-1) awarded to DD. Discussions with Dr. Nicholas Hunter (Monash University) on Quartz CPO analysis were very helpful. Dr. Rüdiger Kilian (University of Halle) and Dr. Ralf Hielscher (TU Chemnitz) are thanked for helping out DD with the usage of MTEX toolbox. Thanks to Prof. Indradev Samajdar (IIT Bombay) for guidance with the EBSD facility. Dr. Trupti Chandrshekar (IIT Bombay) helped with the XRD facility at the Department of Earth Sciences in IIT Bombay. Numerous useful comments made by DD's Ph.D. Committee Members, Prof. George Mathew and Prof. Prabhakar Naraga (IIT Bombay), are appreciated. DD thanks Prof. Saibal Gupta (IIT Kharagpur) and Prof. A. R. Bhattacharya (retired Professor, University of Lucknow) for their valuable inputs on his Ph.D. thesis. We thank Dr. Paris Xypolias (University of Patras) and Dr. Zachary Michels (University of Minnesota) for their thorough and constructive reviews that greatly improved this manuscript. Editorial Handling by Dr. P. Agard (Sorbonne University) is also appreciated. We also thank Mr. Padma Yangjor and Mr. Konchok Dorjay for the field logistics.

Appendix A. Supplementary data

Supplementary data to this article can be found online at <https://doi.org/10.1016/j.tecto.2020.228641>.

References

- Auzanneau, E., Vielzeuf, D., Schmidt, M.W., 2006. Experimental evidence of decompression melting during exhumation of subducted continental crust. *Contrib. Mineral. Petrol.* 152 (125–14).
- Baëta, R.D., Ashbee, K.H.G., 1969. Slip systems in quartz: I. Experiments. *American Mineralogist: Journal of Earth and Planetary Materials* 54, 1551–1573.
- Beaumont, C., Jamieson, R.A., Nguyen, M.H., Medvedev, S., 2004. Crustal channel flows: 1. Numerical models with applications to the tectonics of the Himalayan-Tibetan orogen. *J. Geophys. Res. Solid Earth* 109, B06406.
- Beaumont, C., Jamieson, R.A., Butler, J.P., Warren, C.J., 2009. Crustal structure: a key constraint on the mechanism of ultra-high-pressure rock exhumation. *Earth Planet. Sci. Lett.* 287, 116–129.
- Bestmann, M., Prior, D.J., 2003. Intragranular dynamic recrystallization in naturally deformed calcite marble: diffusion accommodated grain boundary sliding as a result of subgrain rotation recrystallization. *J. Struct. Geol.* 25, 1597–1613.
- Bhattacharya, G., Robinson, D. M., Wielicki, M. M., n.d. Detrital zircon provenance of the Indus Group, Ladakh, NW India: Implications for the timing of the India-Asia collision and other syn-orogenic processes. *Geol. Soc. Am. Bull.* doi:10.1130/B35624.1. In press.
- Bidgood, A.K., Parsons, A.J., Lloyd, G.E., Waters, D.J., Goddard, R.M., 2020. EBSD-based criteria for coesite-quartz transformation. *J. Metamorph. Geol.* <https://doi.org/10.1111/jmg.12566>.

- Bohlen, S.R., Boettcher, A.L., 1982. The quartz - coesite transformation: a precise determination and the effects of other components. *J. Geophys. Res. Solid Earth* 87, 7073–7078.
- Bose, S., Gupta, S., 2020. Evolution of stretching lineations in granulite-hosted ductile shear zones, Eastern Ghats Province, India: Role of temperature, strain rate and pre-existing stretching lineations. *J. Struct. Geol.* 138, 104127.
- Bose, N., Mukherjee, S., 2020. Estimation of deformation temperatures, flow stresses and strain rates from an intra-continental shear zone: the Main Boundary Thrust, NW Himalaya (Uttarakhand, India). *Mar. Pet. Geol.* 112, 104094.
- Bouchez, J.L., Lister, G.S., Nicolas, A., 1983. Fabric asymmetry and shear sense in movement zones. *Geol. Rundsch.* 72, 401–419.
- Buchs, N., Epard, J.L., 2019. Geology of the eastern part of the Tso Moriri nappe, the Nidar Ophiolite and the surrounding tectonic units (NW Himalaya, India). *J. Maps* 15, 38–48.
- Buchs, N., 2019. Geology of the Nidar-Tso Moriri area (Indian Himalayas, Ladakh): From intra-oceanic subduction to nappe exhumation. Unpublished Ph.D. Thesis. Université de Lausanne, p. 246.
- Bundy, F.P., 1980. The P - T phase and reaction diagram for elemental carbon. *J. Geophys. Res. Solid Earth* 85, 6930–6936.
- Bunge, H.J., 1982. *Texture Analysis in Materials Science: Mathematical Models*. London. Butterworth-Heinemann (616 p. ISBN: 978-0-408-10642-9).
- Chamoli, A., Pandey, A.K., Dimri, V.P., Banerjee, P., 2011. Crustal configuration of the northwest Himalaya based on modeling of gravity data. *Pure Appl. Geophys.* 168, 827–844.
- Chatterjee, N., Jagoutz, O., 2015. Exhumation of the UHP Tso Moriri eclogite as a diapir rising through the mantle wedge. *Contrib. Mineral. Petrol.* 169, 1–20.
- Chen, Y.X., Zheng, Y.F., Hu, Z., 2013. Synexhumation anatexis of ultrahigh-pressure metamorphic rocks: Petrological evidence from granitic gneiss in the Sulu orogen. *Lithos* 156, 69–96.
- Cladouhos, T.T., 1999. Shape preferred orientations of survivor grains in fault gouge. *J. Struct. Geol.* 21, 419–436.
- Cloos, M., 1982. Flow melanges: Numerical modeling and geologic constraints on their origin in the Franciscan subduction complex, California. *Geol. Soc. Am. Bull.* 93, 330–345.
- Copley, A., Avouac, J.P., Royer, J.Y., 2010. India-Asia collision and the Cenozoic slowdown of the Indian plate: Implications for the forces driving plate motions. *J. Geophys. Res. Solid Earth* 115, B03410.
- Cross, A.J., Prior, D.J., Stipp, M., Kidder, S., 2017. The recrystallized grain size piezometer for quartz: An EBSD-based calibration. *Geophys. Res. Lett.* 44, 6667–6674.
- Díaz-Azpiroz, M., Fernández, C., Czeck, D.M., 2019. Are we studying deformed rocks in the right sections? Best practices in the kinematic analysis of 3D deformation zones. *J. Struct. Geol.* 125, 218–225.
- Donaldson, D.G., Webb, A.A.G., Menold, C.A., Kylander-Clark, A.R., Hacker, B.R., 2013. Petrochronology of Himalayan ultrahigh-pressure eclogite. *Geology* 41, 835–838.
- Dutta, D., Mukherjee, S., 2019. Opposite shear senses: Geneses, global occurrences, numerical simulations and a case study from the Indian western Himalaya. *J. Struct. Geol.* 126, 357–372.
- Dutta, D., 2020. Opposite Shear Kinematics from the Lesser Himalayan and the Trans-Himalayan terranes, NW India.. PhD thesis IIT, Bombay, p. 510.
- Epard, J.L., Steck, A., 2008. Structural development of the Tso Moriri ultra-high pressure nappe of the Ladakh Himalaya. *Tectonophysics* 451, 242–264.
- Faccenda, M., Gerya, T.V., Chakraborty, S., 2008. Styles of post-subduction collisional orogeny: influence of convergence velocity, crustal rheology and radiogenic heat production. *Lithos* 103, 257–287.
- Faleiros, F.M., Moraes, R., Pavan, M., Campanha, G.A.C., 2016. A new empirical calibration of the quartz c-axis fabric opening-angle deformation thermometer. *Tectonophysics* 671, 173–182.
- Fazio, E., Punturo, R., Cirrincione, R., Kern, H., Pezzino, A., Wenk, H.R., Goswami, S., Mamtani, M.A., 2017. Quartz preferred orientation in naturally deformed mylonitic rocks (Montalto shear zone-Italy): a comparison of results by different techniques, their advantages and limitations. *Int. J. Earth Sci.* 106, 2259–2278.
- Fuchs, G., Linner, M., 1996. On the geology of the suture zone and Tso Moriri dome in Eastern Ladakh (Himalaya). *Jahrbuch Der Geologischen Bundesanstalt* 139, 191–207.
- Giorgis, S., Michels, Z., Dair, L., Braudy, N., Tikoff, B., 2017. Kinematic and vorticity analyses of the western Idaho shear zone, USA. *Lithosphere* 9, 223–234.
- Girard, M., Bussy, F., 1999. Late Pan-African magmatism in the Himalaya: new geochronological and geochemical data from the Ordovician Tso Moriri metagranites (Ladakh, NW India). *Schweiz. Mineral. Petrogr. Mitt.* 79, 399–418.
- Godin, L., Grujic, D., Law, R.D., Searle, M.P., 2006. Channel flow, ductile extrusion and exhumation in continental collision zones: an introduction. In: *Channel flow, ductile extrusion and exhumation in continental collision zones* (Eds: Law R, Searle M P, Godin L). *Geol. Soc. Lond., Spec. Publ.* 268, 1–24.
- Gouzu, C., Itaya, T., Hyodo, H., Ahmad, T., 2006. Cretaceous isochron ages from K-Ar and 40Ar/39Ar dating of eclogitic rocks in the Tso Moriri complex, western Himalaya, India. *Gondwana Res.* 9, 426–440.
- Graziani, R., Larson, K.P., Soret, M., 2020. The effect of hydrous mineral content on competitive strain localization mechanisms in felsic granulites. *J. Struct. Geol.* 134, 104015.
- Grujic, D., Casey, M., Davidson, C., Hollister, L.S., Kündig, R., Pavlis, T., Schmid, S., 1996. Ductile extrusion of the Higher Himalayan Crystalline in Bhutan: evidence from quartz microfabrics. *Tectonophysics* 260, 21–43.
- Guillot, S., de Sigoyer, J., Hattori, K.H., 2000. Mantle wedge serpentinization and exhumation of eclogites: Insights from eastern Ladakh, northwestern Himalaya. *Geology* 28, 199–202.

- Guillot, S., de Sigoyer, J., Lardeaux, J.M., Mascle, G., 1997. Eclogitic metasediments from the Tso Morari area (Ladakh, Himalaya): evidence for continental subduction during India-Asia convergence. *Contrib. Mineral. Petrol.* 128, 197–212.
- Guillot, S., Hattori, K.H., de Sigoyer, J., Nagler, T., Auzende, A.L., 2001. Evidence of hydration of the mantle wedge and its role in the exhumation of eclogites. *Earth Planet. Sci. Lett.* 193, 115–127.
- Hacker, B.R., Ratschbacher, L., Rutte, D., Stearns, M.A., Malz, N., Stubner, K., Kylander-Clark, A.R.C., Pfander, J.A., Everson, A., 2017. Building the Pamir-Tibet Plateau—Crustal stacking, extensional collapse, and lateral extrusion in the Pamir: 3. Thermobarometry and petrochronology of deep Asian crust. *Tectonics* 36, 1743–1766.
- Harris, N., 2007. Channel flow and the Himalayan-Tibetan orogen: a critical review. *J. Geol. Soc.* 164, 511–523.
- Hawemann, F., Mancktelow, N.S., Pennacchioni, G., Wex, S., Camacho, A., 2019. Weak and slow, strong and fast: how shear zones evolve in a dry continental crust (Musgrave Ranges, Central Australia). *J. Geophys. Res. Solid Earth* 124, 219–240.
- Heilbronner, R., Kilian, R., 2017. The grain size (s) of Black Hills Quartzite deformed in the dislocation creep regime. *Solid Earth* 8, 1071–1093.
- Hemley, J.J., Jones, W.R., 1964. Chemical aspects of hydrothermal alteration with emphasis on hydrogen metasomatism. *Econ. Geol.* 59, 538–569.
- Hielscher, R., Schaeben, H., 2008. A novel pole figure inversion method: specification of the MTEX algorithm. *J. Appl. Crystallogr.* 41, 1024–1037.
- van Hinsbergen, D.J., Steinberger, B., Doubrovine, P.V., Gassmoller, R., 2011. Acceleration and deceleration of India-Asia convergence since the cretaceous: Roles of mantle plumes and continental collision. *J. Geophys. Res. Solid Earth* 116, B06101.
- Hippert, J., Tohver, E., 1999. On the development of zones of reverse shearing in mylonitic rocks. *J. Struct. Geol.* 21, 1603–1614.
- Hunter, N.J.R., Weinberg, R.F., Wilson, C.J.L., Luzin, V., Misra, S., 2018a. Microscopic anatomy of a ‘hot-on-cold’ shear zone: insights from quartzites of the Main Central Thrust, Alaknanda Valley (Garhwal Himalaya). *Geol. Soc. Am. Bull.* 130, 1519–1539.
- Hunter, N.J.R., Weinberg, R.F., Wilson, C.J.L., Law, R.D., 2018b. A new technique for quantifying symmetry and opening angles in quartz c-axis pole figures: Implications for interpreting the kinematic and thermal properties of rocks. *J. Struct. Geol.* 112, 1–6.
- Hunter, N.J., Weinberg, R.F., Wilson, C.J.L., Luzin, V., Misra, S., 2019. Quartz deformation across interlayered monomineralic and polymineralic rocks: a comparative analysis. *J. Struct. Geol.* 119, 118–134.
- Johnson, M.R.W., Harley, S.L., 2012. *Orogenesis: The Making of Mountains*. Cambridge University Press, Cambridge, New York (1–388 pp. ISBN: 9781139023924).
- Jones, R.R., Holdsworth, R.E., Clegg, P., McCaffrey, K., Tavarnelli, E., 2004. Inclined transpression. *J. Struct. Geol.* 26, 1531–1548.
- Kilian, R., Heilbronner, R., Stunitz, H., 2011. Quartz microstructures and crystallographic preferred orientation: which shear sense do they indicate? *J. Struct. Geol.* 33, 1446–1466.
- Kronenberg, A.K., Segall, P., Wolf, G.H., 1990. Hydrolytic weakening and penetrative deformation within a natural shear zone. In: Duda, A.G., Durham, W.B., Handin, J. W., Wang, H.F. (Eds.), *The Brittle-Ductile Transition in Rocks*. American Geophysical Union, Washington, pp. 21–36.
- Kruhl, J.H., 1998. Prism- and basal-plane parallel subgrain boundaries in quartz: a microstructural geothermobarometer: Reply. *J. Metamorph. Geol.* 16, 142–146.
- Kurz, W., Fritz, H., Tenczer, V., Unzog, W., 2002. Tectono-metamorphic evolution of the Koralm complex (Eastern Alps): constraints from microstructures and textures of the ‘Plattengneis’ shear zone. *J. Struct. Geol.* 24, 1957–1970.
- Labrousse, L., Jolivet, L., Agard, P., Hebert, R., Andersen, T.B., 2002. Crustal-scale boudinage and migmatization of gneiss during their exhumation in the UHP province of western Norway. *Terra Nova* 14, 263–270.
- Larson, K.P., 2018. Refining the structural framework of the Khimti Kholra region, east-central Nepal Himalaya, using quartz textures and c-axis fabrics. *J. Struct. Geol.* 107, 142–152.
- Larson, K.P., Lamming, J.L., Faisal, S., 2014. Microscale strain partitioning? Differential quartz crystallographic fabric development in Phyllite, Hindu Kush, Northwestern Pakistan. *Solid Earth* 5, 1319–1327.
- Law, R.D., 2014. Deformation thermometry based on quartz c-axis fabrics and recrystallization microstructures: a review. *J. Struct. Geol.* 66, 129–161.
- Leech, M.L., Singh, S., Jain, A.K., 2007. Continuous metamorphic zircon growth and interpretation of U-Pb SHRIMP dating: An example from the Western Himalaya. *Int. Geol. Rev.* 49, 313–328.
- Leech, M.L., Singh, S., Jain, A.K., Klemperer, S.L., Manickavasagam, R.M., 2005. The onset of India-Asia continental collision: early, steep subduction required by the timing of UHP metamorphism in the western Himalaya. *Earth Planet. Sci. Lett.* 234, 83–97.
- Little, T.A., Hacker, B.R., Brownlee, S.J., Seward, G., 2013. Microstructures and quartz lattice-preferred orientations in the eclogite-bearing migmatitic gneisses of the D’Entrecasteaux Islands, Papua New Guinea. *Geochem. Geophys. Geosyst.* 14, 2030–2062.
- Long, S., McQuarrie, N., Tobgay, T., Hawthorne, J., 2011. Quantifying internal strain and deformation temperature in the eastern Himalaya, Bhutan: Implications for the evolution of strain in thrust sheets. *J. Struct. Geol.* 33, 579–608.
- Mainprice, D., Bouchez, J.-L., Blumenfeld, P., Tubia, J.M., 1986. Dominant c slip in naturally deformed quartz: Implications for dramatic plastic softening at high temperature. *Geology* 14, 819–822.
- Maruyama, S., Liou, J.G., Terabayashi, M., 1996. Blueschists and eclogites of the world and their exhumation. *International geology review* 38, 485–594.
- Menegon, L., Pennacchioni, G., Heilbronner, R., Pittarello, L., 2008. Evolution of quartz microstructure and c-axis crystallographic preferred orientation within ductile deformed granulites (Arolla unit, Western Alps). *J. Struct. Geol.* 30, 1332–1347.
- Michels, Z.D., Krukenberg, S.C., Davis, J.R., Tikoff, B., 2015. Determining vorticity axes from grain-scale dispersion of crystallographic orientations. *Geology* 43, 803–806.
- Michibayashi, K., Mainprice, D., 2004. The role of pre-existing mechanical anisotropy on shear zone development within oceanic mantle lithosphere: an example from the Oman ophiolite. *J. Petrol.* 45, 405–414.
- Morgan, S.S., Law, R.D., 2004. Unusual transition in quartzite dislocation creep regimes and crystal slip systems in the aureole of the Eureka Valley–Joshua Flat–Beer Creek pluton, California: a case for anhydrous conditions created by decarbonation reactions. *Tectonophysics* 384, 209–231.
- Mukherjee, S., 2011. Mineral fish: their morphological classification, usefulness as shear sense indicators and genesis. *Int. J. Earth Sci.* 100, 1303–1314.
- Mukherjee, S., 2013. Channel flow extrusion model to constrain dynamic viscosity and Prandtl number of the higher Himalayan Shear Zone. *Int. J. Earth Sci.* 102, 1811–1835.
- Mukherjee, B.K., Sachan, H.K., Ogasawara, Y., Muko, A., Yoshioka, N., 2003. Carbonate-bearing UHPM rocks from the Tso-Morari region, Ladakh, India: petrological implications. *Int. Geol. Rev.* 45, 49–69.
- Mukherjee, S., 2015. A review on out-of-sequence deformation in the Himalaya. In: Mukherjee, S., Carosi, R., van der Beek, P., Mukherjee, B.K., Robinson, D. (Eds.), *Tectonics of the Himalaya*, Geological Society London Special Publications, vol. 412, pp. 67–109.
- Mukherjee, S., Mulchrone, K.F., 2012. Estimating the viscosity and Prandtl number of the Tso Morari crystalline gneiss dome, Indian western Himalaya. *Int. J. Earth Sci.* 101, 1929–1947.
- Najman, Y., Jenks, D., Godin, L., Boudagher-Fadel, M., Millar, I., Garzanti, E., Horstwood, M., Bracciali, L., 2017. The Tethyan Himalayan detrital record shows that India–Asia terminal collision occurred by 54 Ma in the Western Himalaya. *Earth Planet. Sci. Lett.* 459, 301–310.
- Neumann, B., 2000. Texture development of recrystallised quartz polycrystals unravelled by orientation and misorientation characteristics. *J. Struct. Geol.* 22, 1695–1711.
- Okudaira, T., Takeshita, T., Hara, I., Ando, J., 1995. A new estimate of the conditions for transition from basal to prism [c] slip in naturally deformed quartz. *Tectonophysics* 250, 31–46.
- Palazzin, G., Raimbourg, H., Famin, V., Jolivet, L., Kusaba, Y., Yamaguchi, A., 2016. Deformation processes at the down-dip limit of the seismogenic zone: the example of Shimanto accretionary complex. *Tectonophysics* 687, 28–43.
- Palin, R.M., St-Onge, M.R., Waters, D.J., Searle, M.P., Dyck, B., 2014. Phase equilibria modelling of retrograde amphibole and clinzoisite in mafic eclogite from the Tso Morari massif, Northwest India: constraining the P–T–M (H₂O) conditions of exhumation. *J. Metamorph. Geol.* 32, 675–693.
- Palin, R.M., Reuber, G.S., White, R.W., Kaus, B.J., Weller, O.M., 2017. Subduction metamorphism in the Himalayan ultrahigh-pressure Tso Morari massif: an integrated geodynamic and petrological modelling approach. *Earth Planet. Sci. Lett.* 467, 108–119.
- Panozzo, R., Hurlimann, H., 1983. A simple method for the quantitative discrimination of convex and convex-concave lines. *Microsc. Acta* 87, 169–176.
- Passchier, C.W., Trouw, R.A.J., 2005. *Microtectonics*, 2nd Ed. Springer, N. Y. (366 pp. ISBN: 978-3-540-29359-0).
- Pattison, D.R., 1992. Stability of andalusite and sillimanite and the triple point: constraints from the Ballachulish aureole, Scotland. *J. Geol.* 100, 423–446.
- Piette-Lauziere, N., Larson, K.P., Kellett, D.A., Graziani, R., 2020. Intracrystalline vorticity record of flow kinematics during shear zone reactivation. *J. Struct. Geol.* 140, 104134.
- Puelles, P., Abalos, B., Gil Ibarra, J.L., Rodrıguez, J., 2018. Scales of deformation partitioning during exhumation in a continental subduction channel: a petrofabric study of eclogites and gneisses from NW Spain (Malpica-Tui Allochthonous complex). *J. Metamorph. Geol.* 36, 225–254.
- Rai, S.S., Priestley, K., Gaur, V.K., Mitra, S., Singh, M.P., Searle, M., 2006. Configuration of the Indian Moho beneath the NW Himalaya and Ladakh. *Geophys. Res. Lett.* 33, L15308.
- Sachan, B.K., Mukherjee, B.K., Ahmad, T., 2005. Cold subduction of the Indian continental crust: evidence from Tso-morari region, Ladakh, India. *Himal. Geol.* 26, 25–32.
- Schaeben, H., 1988. Entropy optimization in quantitative texture analysis. *J. Appl. Phys.* 64, 2236–2237.
- Schlup, M., Carter, A., Cosca, M., Steck, A., 2003. Exhumation history of eastern Ladakh revealed by 40Ar/39Ar and fission-track ages: the Indus River–Tso Morari transect, NW Himalaya. *J. Geol. Soc.* 160, 385–399.
- Schmid, S.M., Casey, M., 1986. Complete fabric analysis of some commonly observed quartz c-axis patterns. In: Hobbs, B.E., Heard, H.C. (Eds.), *Mineral and Rock Deformation: Laboratory Studies: The Paterson Volume*, Geophysical Monograph, vol. 36, pp. 263–286.
- de Sigoyer, J., Chavagnac, V., Blichert-Toft, J., Villa, I.M., Luais, B., Guillot, S., Mascle, G., 2000. Dating the Indian continental subduction and collisional thickening in the northwest Himalaya: Multichronology of Tso Morari eclogites. *Geology* 28, 487–490.
- de Sigoyer, J., Guillot, S., Lardeaux, J.M., Mascle, G., 1997. Glaucofan-bearing eclogites in the Tso Morari dome (eastern Ladakh, NW Himalaya). *Eur. J. Min.* 10, 1073–1084.
- de Sigoyer, J., Guillot, S., Dick, P., 2004. Exhumation of the ultrahigh-pressure Tso Morari unit in eastern Ladakh (NW Himalaya): a case study. *Tectonics* 23, TC3003.

- Sizova, E., Gerya, T., Brown, M., 2012. Exhumation mechanisms of melt-bearing ultrahigh pressure crustal rocks during collision of spontaneously moving plates. *J. Metamorph. Geol.* 30, 927–955.
- Skemer, P., Katayama, I., Jiang, Z., Karato, S.I., 2005. The misorientation index: Development of a new method for calculating the strength of lattice-preferred orientation. *Tectonophysics* 411, 157–167.
- Steck, A., Epard, J.L., Vannay, J.C., Hunziker, J., Girard, M., Moraro, A., Robyr, M., 1998. Geological transect across the Tso Moarari and Spiti areas: thenappe structures of the Tethys Himalaya. *Eclogae Geol. Helv.* 91, 103–121.
- Stipp, M., Stünitz, H., Heilbronner, R., Schmid, S.M., 2002a. Dynamic recrystallization of quartz: Correlation between natural and experimental conditions. In: De Meer, S., Drury, M.R., De Bresser, J.H.P., Pennock, G.M. (Eds.), *Deformation Mechanisms, Rheology and Tectonics: Current Status and Future Perspectives*, Geological Society, London, Special Publications, vol. 200, pp. 171–190.
- Stipp, M., Stünitz, H., Heilbronner, R., Schmid, S.M., 2002b. The eastern Tonale fault zone: a 'natural laboratory' for crystal plastic deformation of quartz over a temperature range from 250 to 700 °C. *J. Struct. Geol.* 24, 1861–1884.
- St-Onge, M.R., Rayner, N., Palin, R.M., Searle, M.P., Waters, D.J., 2013. Integrated pressure-temperature-time constraints for the Tso Morari dome (Northwest India): Implications for the burial and exhumation path of UHP units in the western Himalaya. *J. Metamorph. Geol.* 31, 469–504.
- Syracuse, E.M., van Keken, P.E., Abers, G.A., 2010. The global range of subduction zone thermal models. *Phys. Earth Planet. Inter.* 183, 73–90.
- Takeshita, T., 1996. Estimate of the physical conditions for deformation based on c-axis fabric transitions in naturally deformed quartzite. *J. Geol. Soc. Japan* 102, 211–222.
- Thakur, V.C., Misra, D.K., 1984. Tectonic framework of the Indus and Shyok suture zones in Eastern Ladakh, northwest Himalaya. *Tectonophysics* 101, 207–220.
- Thakur, V.C., Virdi, N.S., 1979. Lithostratigraphy, structural framework, deformation and metamorphism of the southeastern region of Ladakh, Kashmir Himalaya, India. *Himal. Geol.* 9, 63–78.
- Tikoff, B., Blenkinsop, T., Kruckenberg, S.C., Morgan, S., Newman, J., Wojtal, S., 2013. A perspective on the emergence of modern structural geology: Celebrating the feedbacks between historical-based and process-based approaches. In: Bickford, M.E. (Ed.), *The Web of Geological Sciences: Advances, Impacts, and Interactions*, 500. Geological Society of America Special Paper, pp. 65–119.
- Toy, V.G., Prior, D.J., Norris, R.J., 2008. Quartz fabrics in the Alpine Fault mylonites: Influence of pre-existing preferred orientations on fabric development during progressive uplift. *J. Struct. Geol.* 30, 602–621.
- Vielzeuf, D., Holloway, J.R., 1988. Experimental determination of the fluid-absent melting relations in the pelitic system. *Contrib. Mineral. Petrol.* 98, 257–276.
- Vogt, K., Castro, A., Gerya, T., 2013. Numerical modeling of geochemical variations caused by crustal reamination. *Geochem. Geophys. Geosyst.* 14, 470–487.
- Vollmer, F.W., 1990. An application of eigenvalue methods to structural domain analysis. *Geol. Soc. Am. Bull.* 102, 786–791.
- Weinberg, R.F., Hasalová, P., 2015. Water-fluxed melting of the continental crust: a review. *Lithos* 212, 158–188.
- White, L.T., Lennox, P.G., 2010. Can the size of K-feldspar phenocrysts be used to map the occurrence of mylonitic shear zones? Results from the Wyangala Granite, Eastern Lachlan Fold Belt, New South Wales. *Aust. J. Earth Sci.* 57, 395–410.
- Wibberley, C., 1999. Are feldspar-to-mica reactions necessarily reaction-softening processes in fault zones? *J. Struct. Geol.* 21, 1219–1227.
- Whitney, D.L., Evans, B.W., 2010. Abbreviations for names of rock-forming minerals. *Am. Min.* 95, 185–187.
- Wilke, F.D., O'Brien, P.J., Schmidt, A., Ziemann, M.A., 2015. Subduction, peak and multi-stage exhumation metamorphism: Traces from one coesite-bearing eclogite, Tso Morari, western Himalaya. *Lithos* 231, 77–91.
- Xypolias, P., 2010. Vorticity analysis in shear zones: a review of methods and applications. *J. Struct. Geol.* 32, 2072–2092.
- Xypolias, P., Gerogiannis, N., Chatzaras, V., Papapavlou, K., Kruckenberg, S.C., Aravadinou, E., Michels, Z., 2018. Using incremental elongation and shearing to unravel the kinematics of a complex transpressional zone. *J. Struct. Geol.* 115, 64–81.